Numerical Simulations of Depressurization-Induced Gas Production from an Interbedded Turbidite Gas Hydrate-Bearing Sedimentary Section in the Offshore India: Site NGHP-02-16 (Area-B)

Evgeniy M. Myshakin,[1,2,*] Yongkoo Seol,[1] Jeen-Shang Lin,[1,3] Shun Uchida,[1,4] Timothy S. Collett,[5] Ray Boswell[1]

[1] U.S. Department of Energy, National Energy Technology Laboratory, 626 Cochrans Mill Road, Pittsburgh, PA

[2] AECOM, 626 Cochrans Mill Road, Pittsburgh, PA

[3] Department of Civil and Environmental Engineering, University of Pittsburgh, Pittsburgh, PA

[4] Department of Civil and Environmental Engineering, Rensselaer Polytechnic Institute, Troy, NY

[5] U.S. Geological Survey, Denver, CO

Abstract

The recent National Gas Hydrate Program Expedition 02 (NGHP-02) identified the existence of gas hydrate-bearing sand reservoirs at a number of sites in the offshore of India including Site NGHP-02-16 in Area-B of the Krishna-Godavari Basin. The architecture of that gas hydrate accumulation is characterized by thin, gas hydrate-bearing, high quality sand layers interbedded with mud layers within a turbidite sedimentary interval. The lowest gas hydrate-bearing layer contacting a thinly-interbedded saline aquifer designates the base of the gas hydrate stability zone (BGHSZ). The proximity of the BGHSZ and the average temperature around 20°C make the reservoir a favorable target for hydrate destabilization by means of the depressurization method. The results of the reservoir simulations indicate high gas production potential from this marine gas hydrate deposit with manageable concomitant water production using a well completion design that hydraulically isolates layers with water-saturated sands. Using a detailed geological input model, the predicted cumulative gas rates reach ~3.1 x 10^4 m^3/day (~1.1 MMscf/day) after 90 days of continuous depressurization and demonstrate sustained production rates ~3.0 x 10^4 m^3/day (~1.0 MMscf/day) after 5 years of production. The interbedded nature of this gas hydrate occurrence promotes the development of horizontal dissociation interfaces between gas hydrate-bearing sand and mud layers. As a result, non-uniform gas production along the horizontal interfaces becomes a primary determinant of reservoir performance. Simulation cases have been executed to determine the impact of the uncertainty in *in situ* reservoir permeability and the manner in which intrinsic permeability dynamically changes during dissociation in response to the imposed effective stress increase. The cases based on low initial effective permeability and high sensitivity of compaction to stress result in the least favorable production predictions.

Keywords: gas hydrates; reservoir simulations; marine gas hydrate deposits; India National Gas Hydrate Program

* Corresponding author. Email: evgeniy.myshakin@netl.doe.gov. Tel: 412-386-5741.
626 Cochrans Mill Road, Pittsburgh PA 15236

Introduction

Gas hydrate is widely spread in nature in sub-oceanic sediments, and in permafrost areas and is considered to be a promising future source of energy (Collett et al., 2009). Natural gas production from gas hydrate requires a shift of the pressure and temperature conditions outside of the gas hydrate stability zone on the water-hydrate-gas phase equilibrium diagram to initiate gas hydrate decomposition. The main destabilization methods that induce gas hydrate dissociation include reducing reservoir pressure in the pore space, increasing reservoir temperature, or changing thermodynamic stability conditions through injection of chemical destabilizers (Moridis and Collett, 2004). The depressurization production method is considered to be the most effective method (Moridis et al., 2009; Boswell et al., 2014) that uses both constant-pressure and constant-mass-rate production regimes (Moridis et al., 2004; Kurihara et al., 2008). Since the gas and water flow rates out of the well are subject to time-dependent phase mobilities and the pressure gradient between the production interval of the well and the moving interface boundary, maximizing that pressure gradient is critical for effective depressurization of gas hydrate accumulations. As gas hydrate dissociation continues and the pressure gradient weakens, gas production becomes controlled by sensible heat transfer from surrounding strata (Kowalsky and Moridis, 2007).

In recent years, a number of field-scale drilling and testing programs were conducted at the Mallik research site in Northwest Canada (Dallimore and Collett, 2005; Dallimore et al., 2012), at the Mount Elbert site in Northern Alaska (Hunter et al., 2011; Anderson et al., 2011), in the eastern Nankai Trough, offshore Japan (Yamamoto et al., 2014), in the Bay of Bengal, offshore India (Collett et al., 2014; Kumar et al., 2014), the Ulleung Basin, offshore Korea (Ryu et al., 2013), in the South China Sea, offshore China (Yang et al., 2017) and in the Gulf of Mexico, offshore the United States (Flemings et al., 2017). These programs were successful in confirming the technical viability of gas production from gas hydrate reservoirs through depressurization, and understanding site-specific reservoir petrophysical parameters and details of the geological settings necessary to develop geological input models for reservoir simulations. Numerical simulations provide a low-cost tool to predict the production potential of gas

hydrate-bearing formations utilizing various gas production scenarios, methods, and well designs to support the planning and execution of selected field production projects. With respect to marine hydrate accumulations, recent numerical simulation studies of the gas hydrate response to pressure reduction have delivered valuable information about production potential of gas hydrate sediments in the Gulf of Mexico (Gaddipati and Anderson, 2012; Myshakin et al., 2012), Ulleung Basin in the Korean East Sea (Moridis et al., 2013), the Shensu area in the South China Sea (Zheng et al., 2010), and the eastern Nankai Trough offshore Japan (Kurihara et al., 2008; Zhou et. al., 2014).

The NGHP-02 expedition conducted scientific ocean drilling/coring, logging, and analytical activities to assess and characterize the geological occurrence of gas hydrate deposits along the eastern continental margin of India (Kumar et al., this issue). The expedition prioritized 29 deep offshore sites in the Krishna-Godavari and Mahanadi Basins to identify a suitable site for pilot production testing in a future NGHP-03 expedition. The NGHP-02 expedition discovered world-class gas hydrate accumulations at the Site NGHP-02-16 in Area-B of the Krishna-Godavari Basin; this site contains an attractive formation that can be considered for future gas hydrate production testing. Two potential reservoir systems were identified in Area-B, including an "Upper" Reservoir facies associated with the primarily fine-grained lithologic Units I, II and III and a second "Lower" reservoir section associated with the coarser-grained lithologic Unit IV. The "Upper" Reservoir is characterized by a relatively complex occurrence of both pore-filling and fracture-filling gas hydrates. The Lower Reservoir has proven to be more perspective for highly saturated and thick gas hydrate occurrences. Interpretation of a suite of logging-while-drilling (LWD) data collected at Site NGHP-02-16 (Area-B) confirmed the occurrence of a prospective, highly concentrated 18-m thick gas hydrate interval in the Unit IV reservoir facies (Collett et. al., this issue). Unconsolidated low-permeability muds serve as bounding units to the target reservoir section. The architecture of the gas hydrate accumulation features thin gas hydrate-bearing high quality sand layers interbedded with mud layers within a turbidite sedimentary interval. Laterally, those interval is inferred to be broken by sealing faults, which create no-flow boundaries (Collett et al., this issue). The deepest gas hydrate layer overlies a

thinly-interbedded saline aquifer and is inferred to be in close proximity to the BGHSZ (Waite et al., this issue). The BGHSZ proximity and temperatures around 20 ^{o}C make the reservoir a favorable target for gas hydrate destabilization by means of the depressurization method.

The goal of this study is to provide results and interpretations of reservoir simulations conducted for the interbedded turbidite gas hydrate-bearing sedimentary Unit IV section in Site NGPH-02-16 (Area-B) offshore Eastern India. These simulations were carried out to support ongoing planning for NGHP-03 gas hydrate production testing by providing insight into the potential response of gas hydrate-bearing reservoirs to induced depressurization at a constant bottom hole pressure (BHP) using a conventional well design. Data used to support the modeling have been derived from NGHP-02 acquired well logs, shipboard analysis of conventional and pressure cores, and analyses performed by the National Institute of Advanced Industrial Science and Technology (Yoneda et al., this issue-a; Yoneda et al., this issue-b; Yoneda et al., this issue-c) on NGHP-02 core samples. The set of seismic data from the pre-drill analysis (Shukla et al., this issue) and the LWD data allow estimates of initial conditions and an approximate description of the reservoir extension in the horizontal direction. Using log density-derived porosities, gas hydrate saturations derived primarily from resistivity data, and data from core analysis, a 2D reservoir model was created. Several cases were constructed that address different approaches to geological reservoir characterization, alternative well completion designs, and the uncertainty associated with two key reservoir parameters: initial effective reservoir permeability and the permeability reduction factor associated with sediment compressibility.

1. Geologic Input Model

Details of the geological input models for finely-interbedded sand-mud sequences focusing on Site NGHP-02-16 is presented in Boswell et al. (this issue-a). **Figure 1** depicts the locations of the NGHP-01 and NGHP-02 drill sites including the target Site NGHP-02-16 (Area-B), off the eastern coast of India. Water depth at this location is 2,546.5 m (Kumar et al., this issue). Gas hydrate at Site NGHP-02-16 are hosted within weakly consolidated fine sand and coarse silt sediments interbedded with mud-rich layers.

Figure 2 shows the Two-Way Time (TWT) structural map illustrating the map-view of the NGHP-02 Area-B Lower Reservoir in Unit IV with proposed locations of the fault block boundaries and the test site together with positions of the existing holes.

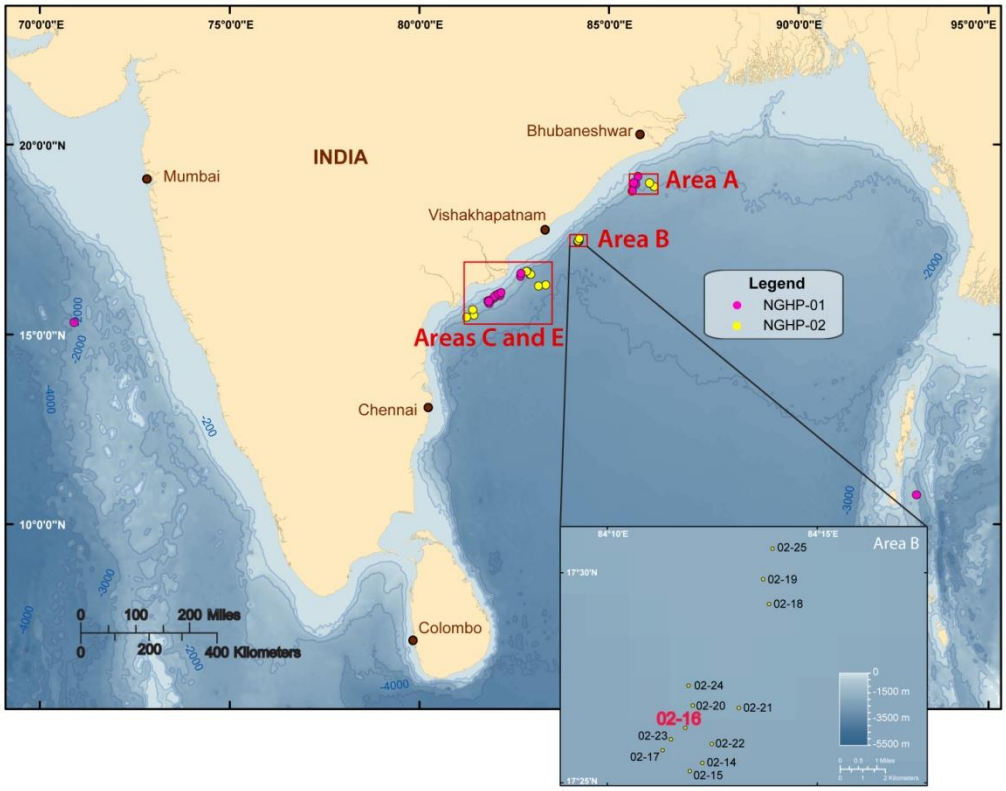

Figure 1. Location of the NGHP-01 and NGHP-02 drill sites, showing Site NGHP-02-16 within "Area-B".

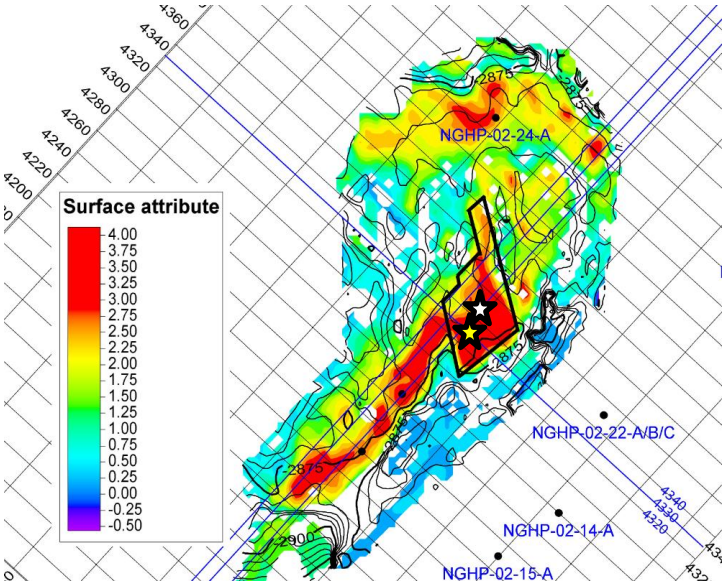

Figure 2. Reservoir top TWT map with root mean squire amplitudes at NGHP-02 Area-B Lower Reservoir (Unit IV). The Site NGHP-02-16 reservoir fault block is defined by the bold black lines. Hole NGHP-02-16A is designated by a yellow star. The proposed location of the test site is shown with the white star.

The drainage area of the reservoir fault block is estimated to be about 560,000 m^2. **Figure 3** represents a composite logging-while-drilling (LWD) log and inferred gas hydrate saturation for the NGHP-02-16A test well showing distinct intervals of the gas hydrate-bearing sand unit (Unit IV) – the Lower Reservoir. Interpretation of log data indicates that gas hydrate saturation can reach 80% of the total pore volume, with bound and free water occupying the rest of the pore volume (Collett et al., this issue). The sediments at Site NGHP-02-16 are divided into five primary model units defined in **Figure 4**. The model built for this study features a detailed stratigraphic representation of the Lower Reservoir and bounding non-reservoir section based on NGHP-02 log data.

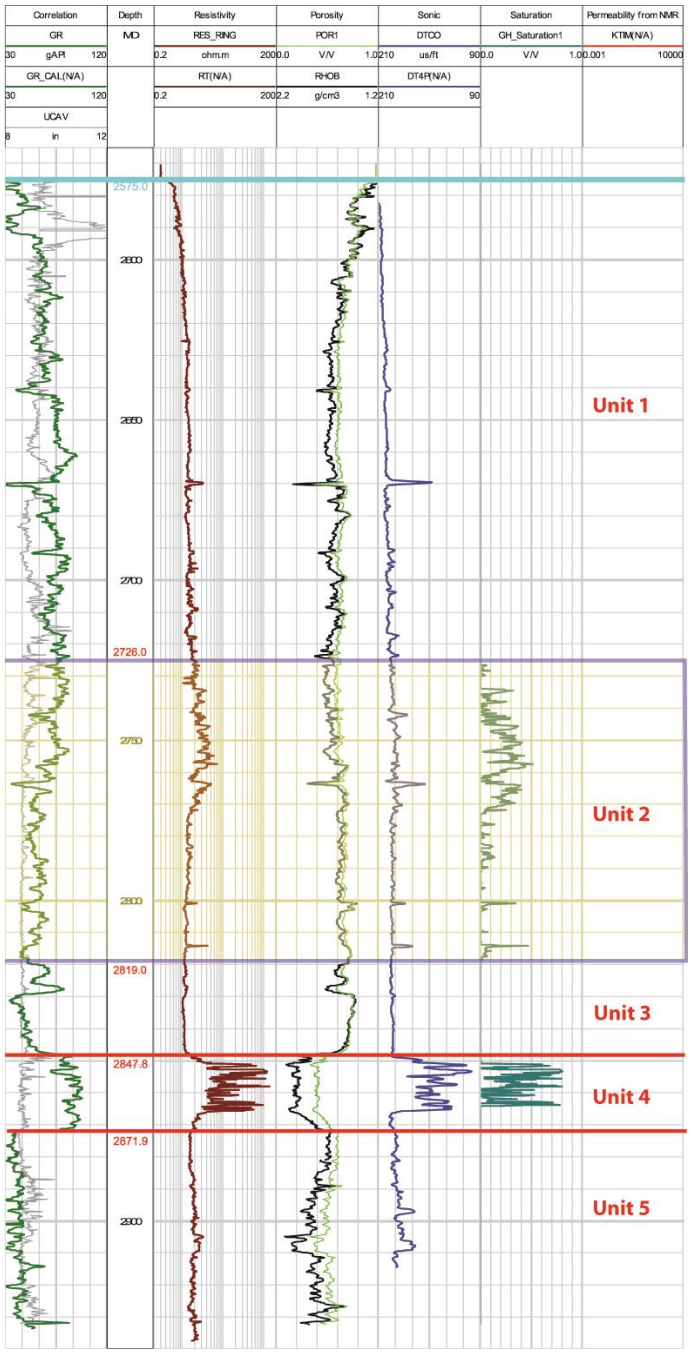

Figure 3. NGHP-02 Area-B reservoir composite well log for the Hole NGHP-02-16A. (from left to right across the plot): i) gamma ray (gAPI, green curve), borehole diameter (inches, grey curve), ii) depth (mbrt, rotary rig table is 28.5 m above sea level), iii) electrical resistivity (Ωm), iv) bulk density (g/cm^3), v) sonic log slowness (us/ft), vi) Archie-resistivity-inferred gas hydrate saturation (fractional), vii) NMR-derived permeability (mD) – no data. The target reservoir interval is the high gas hydrate saturation portion of model Unit 4, also described as lithologic Unit IV, the Lower Reservoir.

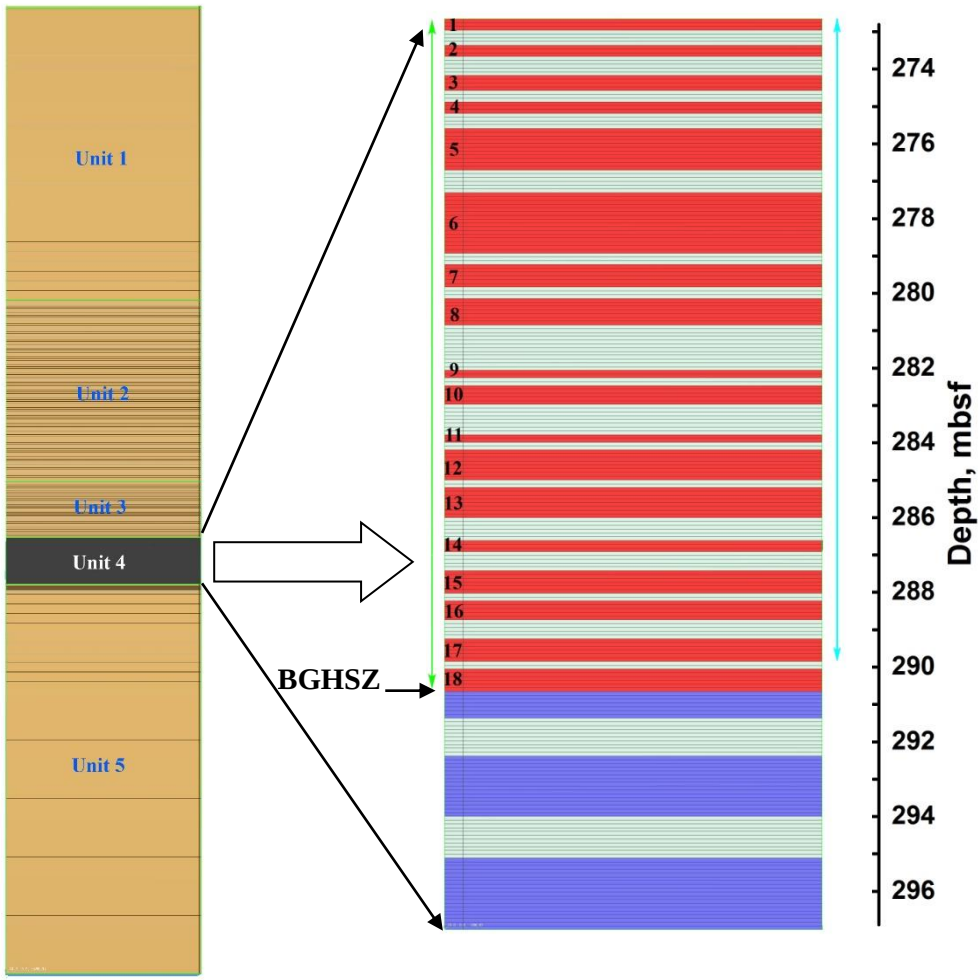

Figure 4. Vertical stratigraphic representation of the model Unit 4 gas hydrate reservoir and bounding non-reservoir sections based on NGHP-02 log data (left). Expanded view of Unit 4 (right) shows detailed sub-unit interpretation. Red – gas hydrate-bearing sand reservoir sub-units (#1-18); Blue – water-bearing sand reservoir sub-units; Gray – non-reservoir mud sub-units. The arrows designate the extension of the production intervals for Cases "1"/"H" (right side arrow) and Cases "2" (left side arrow), respectively.

Figure 4 displays vertical stratigraphic representation of the sediments at Site NGHP-02-16 as inferred from log data and the expanded view of the lower gas hydrate reservoir (model Unit 4, lithologic Unit IV). The unit features eighteen gas hydrate-bearing sub-units interbedded with mud sub-units. The lowermost sub-unit (#18) is in contact with a water-saturated sand sub-unit. The sediments at Site NGHP-02-16 are divided into five primary model units (**Table 1**). The total thickness of the reservoir model is 496.9 m including 24.1 m of the target gas hydrate-bearing Unit 4 reservoir. In the vertical direction, the

mesh discretization contains 404 grid layers of variable thickness with very fine meshing in Unit 4 to provide a detailed description of flow along the boundaries between mud and gas hydrate-bearing sand sub-units.

Table 1. Site NGHP-02-16 gas hydrate reservoir depths and model mesh discretization.

Major model unit	Log measured depth[1] (mbrt)	Sub-seafloor depth[2] (mbsf)	Unit thickness (m)	Thickness of grid layers (m)
UNIT 1: uniform marine mud with no gas hydrate	2,575.0–2,726.0	0.0–151.0	151.0	1 x 31 m 3 x 30 m 6 x 5 m
UNIT 2: uniform marine mud with fracture filled gas hydrate	2,726.0–2,819.0	151.0–244.0	93.0	93 x 1 m
UNIT 3: uniform marine mud with no gas hydrate	2,819.0–2,847.8	244.0–272.8	28.8	36 x 0.8 m
UNIT 4: Interbedded hydrate-bearing sand and gas hydrate-free mud	2,847.8–2,871.9	272.8–296.9	24.1	241 x 0.1 m
UNIT 5: uniform marine mud with no gas hydrate	2,871.9–3,071.9	296.9–496.9	200.0	10 x 0.5 m 9 x 5 m 5 x 30 m
Total	2,575.0–3,071.9	0.0–496.9	496.9	404 variable

[1]Meters below rotary table (rig rotary table above sea level: 28.5 m)
[2]Meters below sea floor (mbsf)

Unit 1 (seafloor to 151 meters below sea-floor (mbsf)) includes high-porosity mud-rich sediments. Unit 1 is modeled using 10 horizontal grid layers of varying thickness (**Table 1**). Unit 2 (151–244 mbsf) represents mud-rich sediment and the occurrence of fracture-filling gas hydrates at relatively low concentration. Unit 2 includes 93 modeled horizontal grid layers, each 1 m in thickness. Unit 3 is a section of uniform marine muds with no gas hydrate occurrence. Unit 3 extends from 244 to 272.8 mbsf and is modeled with 36 individual horizontal grid layers of 0.8 m thicknesses each. The division of Units 1-3 is based on the extent of the gas hydrate occurrence in the overburden of the target gas hydrate reservoir in Unit 4 (**Figure 3**) and does not follow the lithologic unit definitions for which the unit thickness are different (Collett et al., this issue; Jang et al., this issue-a). In the reservoir model, Unit 4 corresponds to lithologic Unit IV and extends from 272.8 to 296.9 mbsf. Sands within Unit 4 below the

depth of 290.6 mbsf, which is interpreted to mark the BGHSZ at this site (Waite et al., this issue), are non-gas hydrate-bearing. Unit 4 includes the reservoir testing target interval and was modeled using 241 horizontal grid layers of 0.1 m thickness that were characterized using two alternative approaches. In CASE 1, these layers were grouped into 40 primary sub-units of average 0.6 m thickness consisting of alternating fine sand and mud (**Figure 5**). Out of 40 sub-units, 18 are assigned as gas hydrate-bearing sand sub-units. CASE 1 assumes a uniform and laterally homogeneous distribution of the physical and hydrological parameters of the reservoir as determined from well log and core data (described below). To provide greater fidelity to the thinly-bedded nature of Unit 4, CASE H was created that assigned unique gas hydrate saturation values to each of 104 gas hydrate-bearing horizontal sand layers with 0.1 m thickness **(Figure 5**). Unit 5 consists of 24 horizontal grid layers of varying thickness that extend from 296.6 to 496.9 mbsf. Unit 5 is a section of uniform marine muds with no gas hydrate present. Unit 5 is assigned an arbitrary thickness of 200 m to provide adequate separation between the primary reservoir interval in Unit 4 and the base of the geologic model. The top of Unit 1 (the seafloor) and the bottom of Unit 5 are set as fixed boundary conditions, with no mass flow allowed across these boundaries. **Table 1** indicates that the reservoir is deep with respect to other known gas hydrate accumulations, with total depth below sea-level of ~2,850 m. At such a depth, and in spite of being so near the base of gas hydrate stability, the reservoir requires a large pressure drawdown to initiate and sustain dissociation. To maximize the pressure gradient, BHP was set at 3.0 MPa, which results in about 25 MPa of pressure drop (Boswell et al., this issue-a). This drawdown will expose the reservoir to large increases in effective stresses that require accounting for the intrinsic permeability change due to pore space reduction. These processes are analyzed in detail by evaluating the reservoir's geomechanical response together with possible fine particle mobilization (Lin et al., this issue; Uchida et al., this issue). A balance between maximizing the pressure gradient and limiting permeability reduction due to sediment compaction might demand less than the maximum pressure reduction. Finding an optimal BHP could be beneficial not only for Site NGHP-02-16, but for assessing ultra-deep marine gas hydrate accumulations in general.

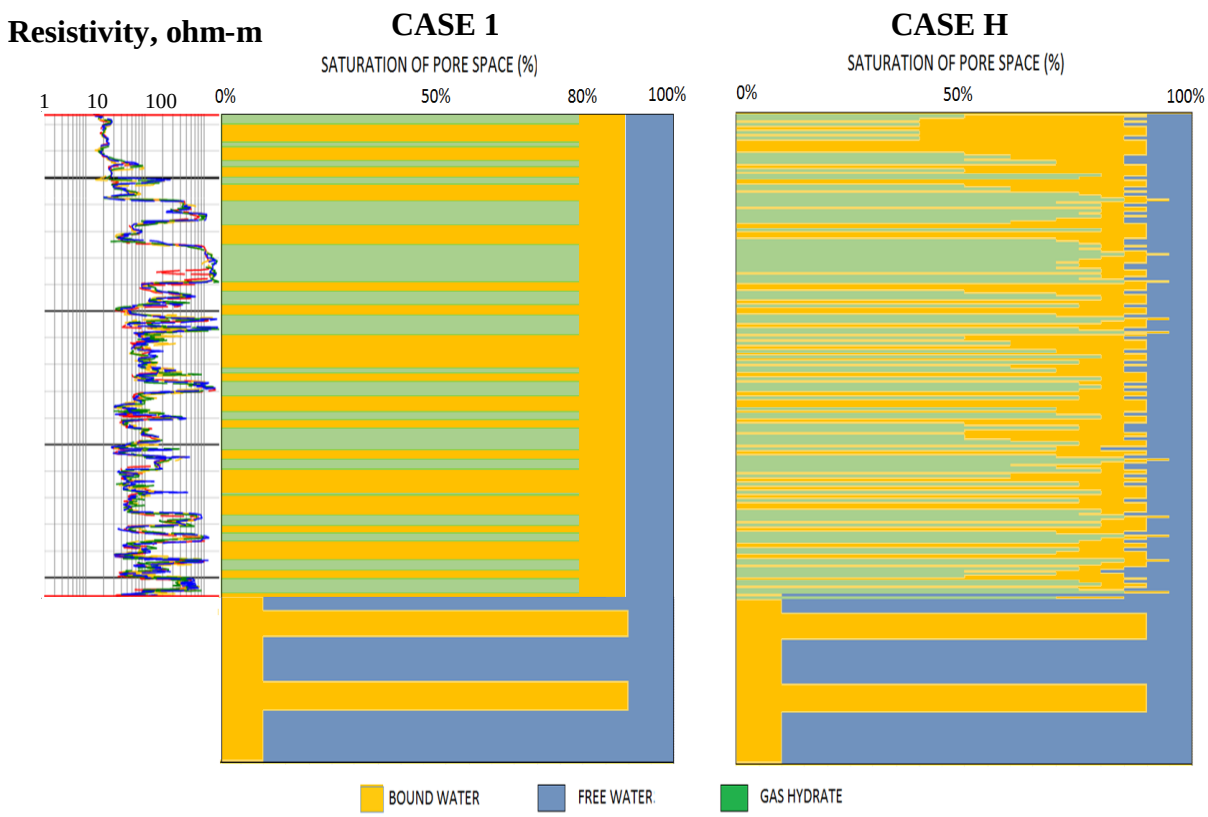

Figure 5. Left: Site NGHP-02-16 resistivity log image. CASE 1: Vertical homogeneous distribution of gas hydrate saturation within each lithology. CASE H: Vertical distribution of gas hydrate saturation with heterogeneous pore fill saturation; gas hydrate saturation (S_{gh}) varies from 40 to 80%, with free water saturation (S_{wf}) ranging from 5 to 20% within the zone of gas hydrate occurrence (Boswell et al., this issue-a).

Geophysical interpretations (Shukla et al., this issue) were used to select the proposed wellbore location and to confirm the lack of any geologic dip or fault compartmentalization within 500 m of that location (the white star in **Figure 2**). Due to this local geologic simplicity, a simplified 2-D geologic input model was deemed suitable, which allowed an efficient analysis of the site. This 2-D model is used to generate 3-D volume results by using cylindrical symmetry and assuming consistent lateral reservoir properties, with a no-flow boundary (representing a lateral boundary related to discrete fault blocks) at 500 m from the wellbore (**Figure 6**). Laterally, the 2-D reservoir is divided into 101 grid blocks with logarithmically increasing lengths with distance from the borehole; the smallest grid block size adjacent to the wellbore is 0.02 m in length. The fine discretization in the near-wellbore region allows the models to appropriately capture details of the fluid flow in the area with the most pronounced physical and

hydrological property changes. Mesh sensitivity analyses were conducted to confirm consistency of reservoir responses to depressurization with finer mesh realizations. Such analyses are an important element of a reservoir model preparation and as shown in Boswell et al. (this issue), using a coarse mesh could grossly underestimate production potential. The model used here has a mesh of 35,904 active elements with 71,354 connections.

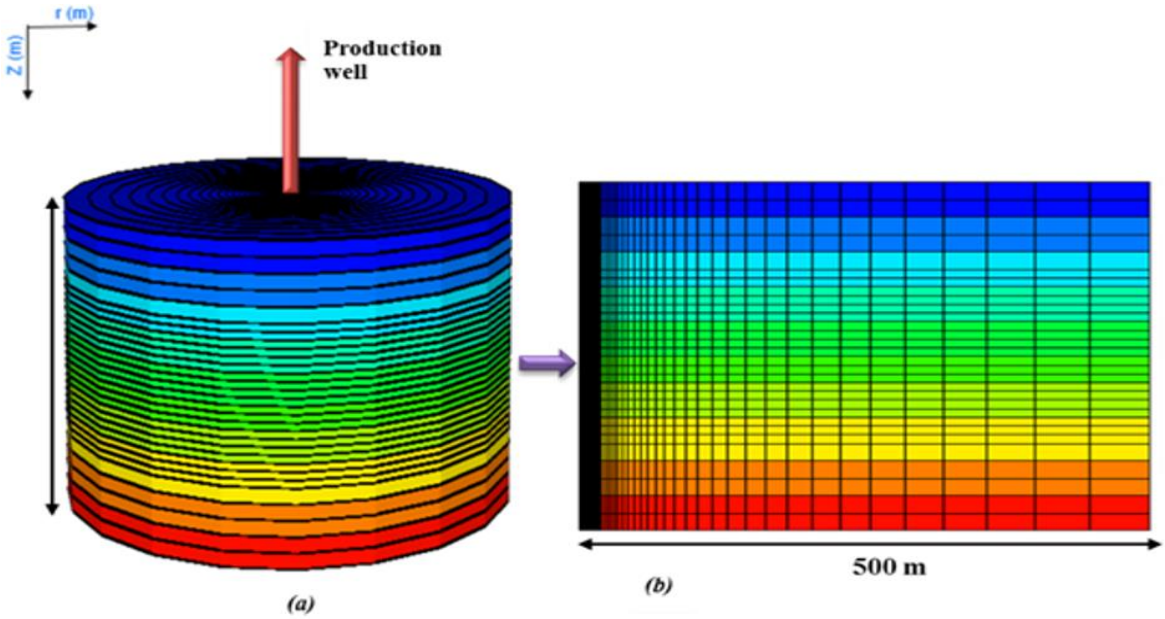

Figure 6. (a) A generalized cylindrical domain representing the gas hydrate reservoir. (b) Radial cross-section of the cylindrical domain with well location along the left edge. Grid block lengths are distributed logarithmically, with smallest cells close to the wellbore. The color scheme is arbitrary.

Simulations of gas production from 2-D models were performed using a parallel version of TOUGH+Hydrate code (Moridis, 2014) developed to model the non-isothermal gas release, phase behavior, and flow of fluids and heat in complex gas hydrate-bearing geological media. The simulator accounts for heat and up to four mass components (water, methane, hydrate, and water-soluble inhibitors) divided between four possible phases (gas, aqueous, ice, and hydrate). The simulator can be used to induce hydrate decomposition by means of depressurization, thermal stimulation, inhibitor addition or a combination of those methods. The thermodynamic equilibrium model is used to describe gas hydrate decomposition into gas and aqueous phases.

2. Reservoir Properties

2.1. Log-Derived Properties for a Thinly-Interbedded Reservoir

Key data used to characterize the gas hydrate bearing units are values for porosity, resistivity, and acoustic wave velocity. These data are primarily obtained from advanced well log suites acquired at Site NGHP-02-16 (Collett et al., this issue). Review of these log data, as well as images and data obtained from NGHP-02 cores, indicates the gas hydrate-bearing units are typically very thin and commonly below the resolution of many of the logging tools (Boswell et al., this issue-a). Because of this complex reservoir architecture, key reservoir properties may not be accurately recorded in the log data; instead, the data represent a composite response of both gas hydrate-saturated sands and the interbedded water-saturated muds. These issues extend to all key petrophysical properties that are calculated from the primary log data. As a result, log-derived estimates in thinly-bedded gas hydrate-bearing sands will characteristically underestimate gas hydrate saturation and overestimate free water saturation in the reservoir sands (Boswell et al., this issue-a). Therefore, geologic interpretation, calibrated where possible to existing core-based measurements, is required to convert log-derived data to those values most likely to represent nature. To accomplish this, we assigned petrophysical parameters to thin beds using two approaches (**Figure 5**). An idealized CASE 1 grouped the gas hydrate-bearing interval in Unit 4 into 18 discrete sub-units ranging from 0.2 to 10.2 m thick (average of 0.6 m). In CASE 1, well log data from several thicker sand reservoir sections, where the log reading was determined to be most accurate, were applied to all sand sub-units within the section regardless of their thickness. A second, more detailed CASE H, recognized more than 100 gas hydrate-bearing sub-units, and assigned to these units a range of reservoir saturations designed to capture the expected variation and linkages between saturations of gas hydrate, free water, and bound water (**Figure 5**). The detailed description of saturation assignment is provided in Section 2.4 below. These alternative geologic input models incorporate insights gained from the analyses of NGHP-02 cores (Yoneda et al., this issue-a; Yoneda et al., this issue-b; Yoneda et al., this issue-c). While log data is the primary data source as it represents a continuous downhole measurement of

properties, cores only yield data for isolated depth locations and the precise depth tie between any core measurements and the log data is difficult to determine. Furthermore, it is important to critically assess the relevance of any core data for application to the modeling of generalized geologic units in a simulation model. For example, a small sample acquired from a relatively thick sand unit could be impacted by inclusions of minor mud interbeds.

2.2. Initial Pressure and Temperature Conditions

The BGHSZ is interpreted to occur within Unit 4 (at the base of sub-unit #18 in CASE 1, **Figure 4**) at 290.6 mbsf (Waite et al., this issue). We assume that pressure follows a hydrostatic gradient. Temperature is determined by using a temperature gradient of 0.0663 °C/m with a sea-floor temperature of 1.9855 ^{o}C (Collett et al., this issue). The water salinity was set at 35 ppt and a salinity correction to the methane-water-methane hydrate equilibrium curve was applied using the equation of Dickens and Quinby-Hunt (Dickens and Quinby-Hunt, 1997). Given these assumptions, conditions at the BGHSZ at Site NGHP-02-16 are estimated as 28.73 MPa and 19.89 °C (see **Section S1** in Supplemental Materials). For the grid layers of the reservoir model, an initialization of initial P/T conditions (pressure and temperature gradients throughout the vertical dimension of the domain) was carried out to achieve hydraulic, thermal, thermodynamic, and chemical equilibrium and ensure correct location of the layers relative to the BGHSZ.

2.3. Porosity

Porosity of all gas hydrate-bearing sand-rich units was set at 40% in both CASE 1 and CASE H, this value is well-aligned with log-based porosity measurements for the thicker sand units (**Figure 3**) and with measurements obtained for silty-sand and sandy-silt cores of Unit 4 (Yoneda et al., this issue-a).

2.4. Phase Saturation

Log-based estimate of gas hydrate saturations (S_{gh}) were typically 80% for the thicker sands units, and this value was applied to all sand layers in CASE 1. This value is similar in other gas hydrate systems

worldwide, and with both NGHP-02 log (Collett et al., this issue) and core data (Yoneda et al., this issue-a; Yoneda et al., this issue-b; Yoneda et al., this issue-c; Boswell et al., this issue-b). Of the remaining 20% of pore space, we assign half to mobile ("free") water (S_{wf}) and half to bound water (S_{wb}), so that S_{gh} = 80%; S_{wf} = 10%; S_{wb} = 10%. While it has been observed that these phase saturations are closely linked (that is, decreases in S_{gh} generally equate to increases in S_{wb}), it is well-recognized that some minor variation in the ratio of these saturations occurs at small scales (Boswell et al., 2017). It is further recognized that variation in the intrinsic reservoir quality of the sand units occurs (Ajayi et al., 2018). While the log data resolution is not sufficient to fully document these variations, we have attempted to capture this expected heterogeneity using CASE H. In this case, S_{gh} is most commonly 80%, but is allowed to vary from 70 to 85% within those units that are allocated an intrinsic permeability (K_{int}) of 1000 mD. Likewise, S_{wf} varies from 5% to 15% with the remainder belonging to bound water. Further, a small number of transitional (e.g., sandy-silt or clay-rich sand) units with S_{gh} as low as 40% (with S_{wf} = 15% and S_{wb} = 45%) are assumed to occur – these units are assigned K_{int} of 500 mD. Within Unit 4, the interbedded muds are uniformly characterized as follows: S_{gh} = 0% with S_{wf} = 10% and S_{wb} = 90%. The degree of this heterogeneity in phase saturations was set somewhat arbitrarily, but was guided by the principle that phase saturations are closely, but not entirely, linked to the grain size and mineralogy of the host sediment, and therefore also to sediment pore size, pore connectivity, and permeability (Torres et al., 2008; Fujii et al., 2009; Collett et al., 2009; Boswell et al., 2016). The interdependency between initial gas hydrate, free water, and bound water saturations reflects the quality of host sediment that translates the predominance of coarse particles into high gas hydrate/low bound water saturations and fine particles enriched with clays and other hydrophilic minerals into low gas hydrate/high bound water saturation values. However, it is recognized that, within any given hydrate accumulation, variation in saturation for all these phases can be driven by multiple causes and that the relationships stated above are not likely to be perfect. The resulting heterogeneity between gas hydrate-bearing sands, particularly with respect to free water saturation, may have a profound impact on reservoir response to depressurization (Ajayi et al., 2018), and CASE H was designed to test this. In CASE 1 and CASE H, the total gas volumes in the gas

hydrate phase and dissolved in liquid phase are 1.81 x 10^9 and 1.77 x 10^9 m^3 (standard conditions: 1 atm and 15^0 C), respectively.

2.5. Permeability and Capillary Pressure

Permeability is a key parameter that determines the ability of fluids to flow through a reservoir; therefore, appropriate assignment of permeability values is critical for reliably predicting reservoir behavior (Moridis et al., 2009). Numerous works have been devoted to determining permeability from both laboratory studies (Kneafsey et al., 2011; Konno et al., 2015; Yoneda et al., this issue; Dai et al., this issue; Jang et al., this issue-a; Boswell et al., this issue-b) and calibration to available field data (Anderson et al., 2011; Uddin et al, 2012; Konno et al., 2017).

In this work, the Brooks-Corey equation (Brooks and Corey, 1964) was used to calculate relative permeabilities of mobile phases (**Equation 1**). The relative permeabilities of aqueous and gas phases are used to compute the corresponding effective permeabilities (**Equation 2**).

$$K_{r\beta} = \left\{ \frac{(S_\beta - S_{\beta b})}{(1 - S_{wb} - S_{gb})} \right\}^{n_\beta} \tag{1}$$

$$K_{eff,\beta} = K_{r\beta} K_{int} \tag{2}$$

where, β is aqueous (w) or gas (g) phases; $K_{r\beta}$ is relative permeability of the mobile phase; S_β is (total) saturation of w or g phases; $S_{\beta b}$ is bound saturation of w or g phases; n_β is the Brooks-Corey exponent for w or g phases; $K_{eff,\beta}$ is effective permeability of mobile phase, β; K_{int} is intrinsic (or absolute) permeability of the reservoir.

Pore space is divided between hydrate, aqueous, and gas phases, so $S_{gh} + S_w + S_g = 1$. Consequently, reduction of hydrate saturation due to dissociation is directly accounted for in the Brooks-Corey model to estimate relative permeability for mobiles phases. The alternative approach implies an intrinsic permeability reduction due to the presence of solid phases (such as ice or gas hydrates). Then, estimations of relative permeabilities are performed using saturations in effective pore space occupied by mobile

phases only. That approach was not considered in this study due to the absence of reliable data that could be used to calculate the intrinsic permeability reduction as a function of gas hydrate saturation.

Before production, permeability of the target reservoir units hosting gas hydrate in the pore space is called initial (aqueous) effective permeability ($K_{ieff,w}$). In **Equation 1** the exponent n_w is set to generate a required initial effective permeability, $K_{ieff,w}$ at a given K_{int}. Thus, the exponent n_w is set at 2.1 to get the initial effective permeability, $K_{ieff,w}$, equal to 10 mD (mD = milliDacry = 9.869×10^{-16} m^2) for the high-permeability cases and set at 4.2 to get $K_{ieff,w}$ = 0.1 mD for the low-permeability cases (Table 6). Both cases assume an initial gas hydrate saturation of 80%, intrinsic permeability of 1000 mD, and irreducible (bound) aqueous pore-space saturation of 10%. The exponent value for gas, n_g = 3.16 is used for all cases, which is the value deduced for the Brooks-Corey model at the gas hydrate saturation of 40%, and is a median number for the 2.7-3.5 range as reported by Mahabadi et al. (2016). The irreducible gas, or bound gas saturation (S_{gb}) is assumed to be zero.

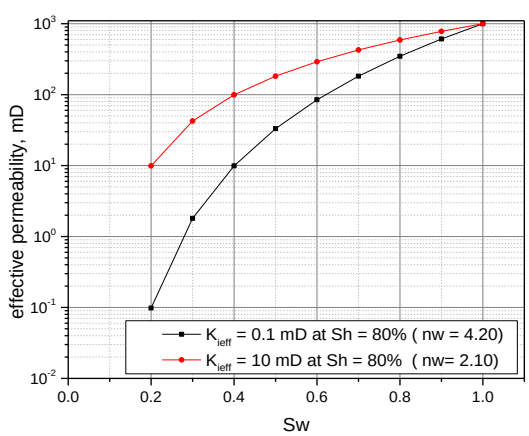

Figure 7. The red curve shows the relationship between total water saturation (S_w) and aqueous effective permeability for CASE 1, CASE H, and CASE 2 with K_{int} = 1000 mD and $K_{ieff,w}$ = 10 mD. The black curve shows the relationship for CASE 1b and CASE Hb with K_{int} = 1000 and $K_{ieff,w}$ = 0.1mD.

Figure 7 displays the effective permeability dependence as a function of aqueous saturation for two values of the exponent n_w (CASE 2, CASE 1b, and CASE Hb will be discussed later in the text). It should

be recognized that permeability varies with direction. Permeability is typically highest when measured horizontally (parallel to bedding) and lowest when measured vertically. In our modeling, this ratio is set at 10:1, which is similar to general assumptions in the majority of numerical simulation studies on gas hydrate. However, a $K_{ieff,w}$ measurement for one NGHP-02 core sample (16B-4P 277.22-277.30 m silty sand core with S_{gh} = 72%) suggests that the ratio may locally be as low as 4:1 (Yoneda et al., this issue-a). A second specimen from the same gas hydrate reservoir, but collected at the NGHP-02-23 well, yielded a permeability anisotropy of 4.24:1 (Dai et al., this issue). Perhaps, in future studies the anisotropy ratio can be assumed to be closer to 5:1, which was adopted in the study done to history-match gas production data at the Mallik 2L-38 site (Uddin et al., 2012).

Measured vertical K_{int} associated with Site NGHP-02-16 reservoir facies range from 0.03 – 190 mD (Yoneda et al., this issue-a); we assess the low value to reflect the mud facies and the high value to reflect the sand/silt facies. In the simulations, the K_{int} of sand units is set at 1000 mD (horizontal) and 100 mD (vertical). In CASE H, an intermediate horizontal K_{int} = 500 mD is set for selected transitional layers between mud and sand. In the text, initial effective permeability refers to permeabilities in the horizontal direction unless otherwise specified. $K_{ieff,w}$ is set at 10 mD in CASE 1, which is aligned with the values that have been reported from NGHP-02 pressure core studies (about 8 mD for horizontal permeability, Yoneda et al., this issue-a;) and used in modeling the Nankai Trough gas hydrate deposit (Konno et al., 2017). In CASE H, the exponential parameter of the relative permeability function is the same as for CASE 1. Since the initial gas hydrate saturations, as well as the free and bound water saturations vary across the sub-units, $K_{ieff,w}$ varies as well ($K_{ieff,w}$ equals 10 (horiz.) and 1 (vert.) mD only for those grid layers with S_{gh} = 80%, S_{wf} = 10%, and S_{wb} = 10%). Alternative cases (CASE 1b, CASE Hb) designate low initial effective permeability ($K_{ieff,w}$ equals 0.1 (horiz.) / 0.01 (vert.) mD) to accommodate variability in that parameter. Dai et al. (this issue) have measured horizontal $K_{ieff,w}$ equals 0.96 mD in the core sample with 80% of gas hydrate saturation from the Area B (Site NGHP-02-23). The lower boundary of initial effective (vertical) permeabilities for NGHP-02 pressurized core samples is 0.007 mD (Yoneda et al., this

issue-a), which translates about 0.1 mD for the horizontal permeability using the assumed 10:1 anisotropy ratio. In all models, the interbedded mud sub-units in Unit 4 were assigned uniform porosity (40%). To relate porosity and intrinsic permeability, experimental permeability measurements of clayey samples from the Nankai Trough site (Nishio et al., 2009) were used with an assumption that those sediments are similar in nature to Site NGHP-02-16 muds. Using the permeability-porosity relation derived from the clayey samples, values for the muds in Unit 4 were set such that K_{int} equal to 0.05 (horiz.) and 0.005 (vert.).

The two-phase flow in porous media of a dissociating gas hydrate reservoir requires accounting for the capillary pressure. The capillary pressure model used in the simulations employs the van Genuchten function (van Genuchten, 1980) with parameters deduced from experiment (Anderson et al., 2011).

$$P_{cap} = -P\left[(S_W{}^*)^{-1/\lambda} - 1\right]^{1-\lambda} \tag{3}$$

where, $S_W^* = \frac{(S_W - S_{Wb})}{(1 - S_{Wb})}$ (4)

S_w – total aqueous saturation, S_{wb} – bound water saturation, λ=0.77437; $P = 10^3$ Pa.

2.6. Pore Compressibility and Intrinsic Permeability Change

Withdrawing fluids through a borehole causes a pore pressure decrease within the reservoir and an effective confining stress increase that, in turn, results in sediment compaction and intrinsic permeability reduction. The effect of pressure change on the matrix porosity is described by the following equation:

$$\phi = \phi_0 F_{PT}; \quad F_{PT} = \exp\left(\alpha_P \Delta P + \alpha_T \Delta T\right) \tag{5}$$

where ϕ is porosity, $\Delta P = P - P_0$ is the imposed pore pressure change, $\Delta T = T - T_0$ is the resulting temperature change, and the index "*0*" designates a reference state. The coefficient α_P is the pore compressibility (1/Pa) that is approximated to be a constant throughout dissociation and α_T is thermal expansivity of the porous media (1/K) that is assumed to be negligible and is not considered in this study.

The ϕ - K_{int} relationship in the matrix is described by the general expression below (Rutqvist and Tsang, 2002):

$$\frac{K_{int}}{K_{int}^{0}} = exp\left[\gamma\left(\frac{\phi}{\phi_0} - 1\right)\right] \quad (6)$$

where gamma, γ, is an empirical permeability reduction factor connecting the porosity change with the intrinsic permeability change.

The modeled values for pore compressibilities of sand and mud sediments were validated using the results of geomechanical experiments for Site NGHP-02-16 core samples (Yoneda et al., this issue-b; Yoneda et al., this issue-c) and by applying a sub-loading critical state model for methane hydrate bearing soils (Uchida et al, 2012). The pore compressibility values are estimated to be α_P= 1.3 x 10^{-8} Pa^{-1} for sand and 8.5 x 10^{-8} Pa^{-1} for mud. Details of the analysis can be found in Lin et al. (this issue). Using the available Site NGHP-02-16 core data obtained by Transparent Acrylic Cell Triaxial Testing (TACTT) (Yoneda et al., this issue-b; Yoneda et al., this issue-c), γ may be as high as 17.2, which equates to a two orders of magnitude reduction in permeability and a porosity drop from 40% to 30% (**Figure 8**: left panel). At high effective confining stress the samples likely experience grain crushing as shown by Bolton et al. (2008) and inferred by Kim et al. (this issue) and Yoneda et al. (this issue-a). Grain crushing would greatly reduce permeability and contribute to a high γ value. However, if that process is a major contributor, the permeability – porosity dependency shown in **Figure 8** (left panel) would be non-linear with more pronounced sensitivity of permeability to lower porosity values (higher stresses). An alternative permeability-porosity dependency is based on the classical Kozeny-Carman equation which yields a γ value of 4.6 (**Figure 8** (right panel)). That value indicates that using the Kozeny-Carman equation probably tends to underestimate the permeability sensitivity on sediment compaction for these deep reservoirs. In our modeling, we have used γ = 4.6 in CASE 1 and CASE H. Alternative runs (case "x") utilizing γ = 17.2 are named CASE 1x and CASE Hx.

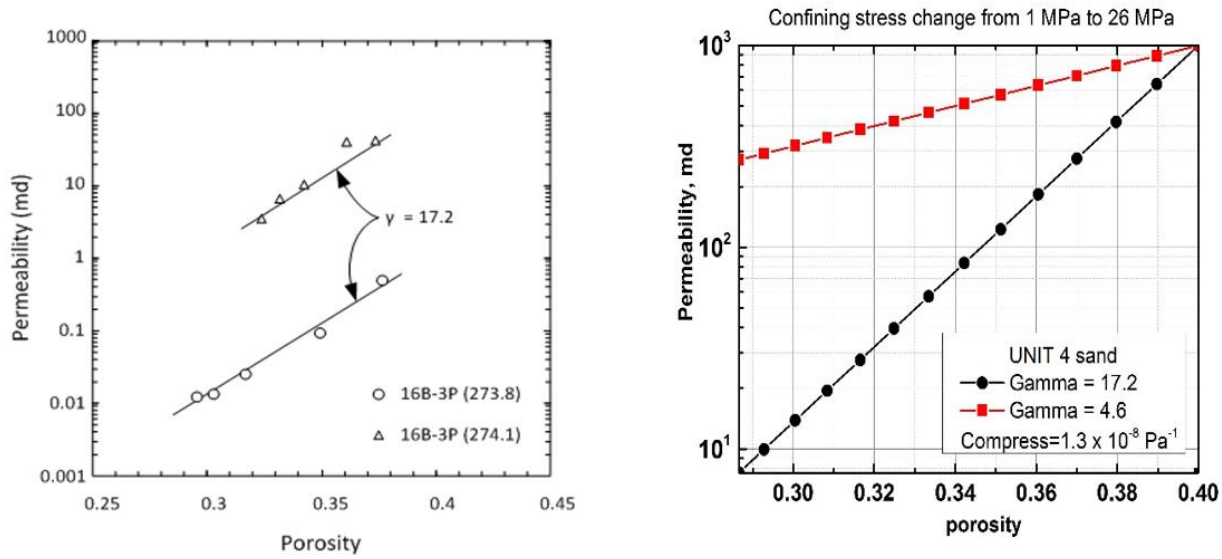

Figure 8. Left: Initial effective (vertical) permeability development due to porosity change induced by effective confining pressure change for two samples from core 3P taken at NGHP-02-16 (Yoneda et al., this issue-a; Yoneda et al., this issue-b; Yoneda et al., this issue-c). For both samples, the slope of the relationship indicates a value for γ = 17.2. Right: alternative relationship assuming no grain crushing yields γ = 4.6.

The interbedded mud layers, to which we assign a non-zero K_{int} and no gas hydrate saturation, undergo their own evolution due to fluid withdrawal and compaction. There are no consolidation tests performed on NGHP-02 cores taken from mud Units 1-3, 5 and mud sub-units of Unit 4. Therefore, the permeability–porosity correlation is taken from measurements obtained from clay-rich Nankai Trough samples (Nishio et al., 2009) (**Figure 9**) to derive the γ value equal to 6.8. That value was used to estimate permeability reduction in response to sediment compaction for mud units and sub-units.

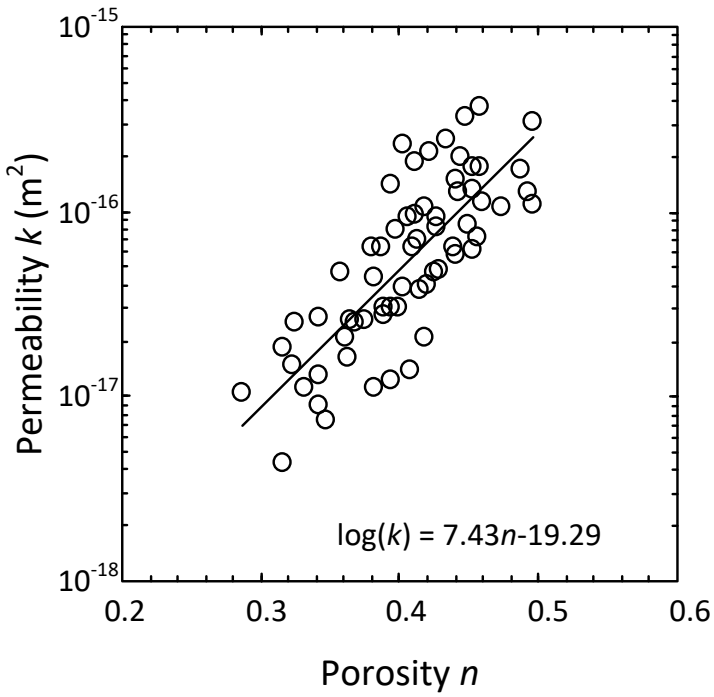

Figure 9. Cross-plot of K_{int} and porosity for clay-rich sediments from the Nankai Trough (from Nishio et al., 2009).

2.7. Thermal Conductivity

Thermal conductivity of the host reservoir is one of the key factors that controls reservoir productivity (Ajayi et al., 2018). Within a self-contained fault block such as that inferred for Site NGHP-02-16, conductive heat transfer from rock matrix to dissociation interface within the pore space and convection of heat related to the lateral movement of fluids in response to depressurization (Yamamoto et al., 2017) are major sources of heat that are needed to sustain gas hydrate dissociation. The composite thermal conductivity (k_θ) used in the simulations to compute heat transfer varies due to changes not only in porosity and saturations, but with mineralogy as well. We use mineralogy data of Site NGHP-02-16 gas hydrate-bearing cores (**Table 2**) to estimate k_θ of bulk sediments. The mineralogy of sand-rich and clay-rich Site NGHP-02-16 gas hydrate-bearing cores were used to determine k_θ for reservoir sand and mud sub-units, and for mud units. The procedure uses a linearly-weighted average of the thermal conductivities for the various minerals (**Table 2**). Three mixing methods for calculating k_θ were compared

with the averaged experimental thermal conductivity value based on the measurements of Site NGHP-02-16 gas hydrate-bearing cores (**Table 3**). For each method, dry ($k_{\theta d}$, 100% of pore space is occupied by gas) and wet ($k_{\theta w}$, 100% of pore space is occupied by water) thermal conductivities were estimated assuming k_{rock} = 5.60, $k_{gashydrate}$ = 0.6 (Waite et al., 2007), k_{water} = 0.6 (Touloukian et al., 1970), and k_{metane} = 0.07 W/m K (Friend and Ely, 1989).

Table 2. Mineral compositions of the sand-rich and clay-rich Site NGHP-02-16 cores* and corresponding mineral thermal conductivity (*k*).**

Mineral	% content sand-rich / clay-rich	*k* (W/m·K)
Quartz	49 / 35	8.27
Calcite	14 / 15	3.4
Plagioclase	7 / 5	1.8
Smectite	6 / 16	1.8
Chlorite	6 / 9	1.9
Mica	4 / 3	2.3
Kaolinite	4 / 3	2.8
Dolomite	3 / 2	5.1
Orthoclase	3 / 2	2.3
Hornblende	2 / 0	2.9
Pyrite	1 / 1	19.2
Siderite	1 / 9	5.1
Total rock	100	5.60 sand-rich / 4.40 clay-rich

***** Yoneda et al., this issue-c; **Clauser and Huenges, 1995; Midttømmeet et al., 1998

Table 3. Comparison of calculated composite thermal conductivity (k_θ with the averaged measured thermal conductivities of Site NGHP-02-16 gas hydrate-bearing pressurized cores (*Aver.* k_{exp}) at the NGHP-02-16B-3P and NGHP-02-16B-7P core depths in Unit 4.*

Interval (mbsf)	ϕ (%)	S_{gh} (%)	k_{exp} (W/m K)		*Aver.* k_{exp} (W/m K)
16B-3P (274.33-274.37)	45.9	75.9	1.969		
16B-3P (273.98-274.03)	45.7	74.5	1.702		**1.720**
16B-7P (287.26-287.34)	46.9	77.6	1.487		
Model	*Aver.* ϕ (%)	*Aver.* S_{gh} (%)	$k_{\theta d}$ (W/mK)	$k_{\theta w}$ (W/mK)	k_θ ** (W/mK)
Maxwell (Maxwell,1954)	46.2	76.0	0.30	1.79	**1.79**

Anand (Anand et al.,1973)	46.2	76.0	0.46	1.76	**1.63**
Somerton (Somerton,1992)	46.2	76.0	0.46	1.76	**1.76**

*Muraoka et al., this issue-c; **pore space is divided between hydrate and water (76% and 24%, respectively)

The closest match with the averaged experimental thermal conductivity value was provided by the Somerton model (Somerton, 1992). That method was used in the simulations and the corresponding equation for k_θ is given below:

$$k_\theta = k_{\theta d} + (S_w + S_{gh})(k_{\theta w} - k_{\theta d}) + \phi S_I k_{\theta I} \quad (7)$$

where S_w , S_{gh} , and S_I are aqueous, hydrate, and ice (it is zero in this study) saturations, respectively; $k_{\theta d}$, $k_{\theta w}$, and $k_{\theta I}$ are dry, wet, and ice thermal conductivities, respectively; ϕ is porosity.

2.8. Pertinent Reservoir Parameters

Key modeling parameters used in the simulations are summarized in **Tables 4** and **5**.

Table 4. Site NGHP-02-16 initial reservoir properties for different lithologies in Unit 4 (CASE H and CASE 1)

Unit 4	ϕ (%)	S_{gh}(%)	S_{wf}(%)	S_{wb}(%)	$K_{ieff,w}$ horiz. (mD)	$k_{\theta d}$ /$k_{\theta w}$ (W/m K)	α_p (Pa^{-1})	γ	rock density (kg/m^3)
GH-sand CASE 1	40	80*	10*	10*	10	0.56/1.94	1.3x10^{-8}	4.6	2,750
GH-sand CASE H	40	40-85	5-15	10-40	10	0.56/1.94	1.3x10^{-8}	4.6	2,750
muds	40	0	10	90	0.05	0.35/1.73	8.3x10^{-8}	6.8	2,750
H_2O-sat. sand	40	0	90	10	1000	0.56/1.94	1.3x10^{-8}	4.6	2,750

***For CASE H, saturation values vary every 0.1 m of depth (see **Figure 5**)

Table 5. Site NGHP-02-16 initial sediment parameters for non-target units (CASE H and CASE 1)

Unit	ϕ (%)	S_{gh}(%)	S_{wf}(%)	S_{wb}(%)	$K_{ieff,w}$ horiz. (mD)	$k_{\theta d}/k_{\theta w}$ (W/m K)	α_p (Pa^{-1})	γ	rock density (kg/m^3)
1	67	0	10	90	4.88	0.25/1.24	8.3x10^{-8}	6.8	2,750
2	66	10	10	80	4.11	0.26/1.25	8.3x10^{-8}	6.8	2,750
3	71	0	10	90	9.67	0.23/1.19	8.3x10^{-8}	6.8	2,700
5	53	0	10	90	0.44	0.35/1.44	8.3x10^{-8}	6.8	2,650

3. Well Design

In both CASE H and CASE 1, the Site NGHP-02-16 production test well is modeled as a vertical well with an open hole completion with assumed perfect sand control (the wellbore is a no-flow boundary for sand) from 272.8 to 289.8 mbsf (Unit 4 sand sub-units #1 to 17 and interbedded mud sub-units of CASE 1, **Figure 4**). In both cases, the gas hydrate-bearing sands and the mud-rich interbeds are free to communicate with the wellbore. This design leaves the basal gas hydrate-bearing sand, its overlying thin mud layer, and all subjacent water-bearing sub-units with no direct connection to the wellbore. This design was selected in order to isolate the well from the water-bearing, high-permeability sub-units below the BGHSZ as these units can greatly complicate the ability to reduce borehole pressure if they are not well confined, Moridis et al., 2009), and can also be a prolific source of sediment and water production into the well completion (Konno et al., 2017). The cases described below with the number "1" in their names use this well completion.

The alternative cases designated with the number "2" were conducted to examine the production potential should the aquifer be open to the well with a condition that the bounding faults of Site NGHP-02-16 fault block effectively seal the unit and allow no external flow of water into the fault block. If such communication does exist, (which may be likely), the ability to depressurize the reservoir would be greatly curtailed (Boswell et al., 2009). These alternative cases assume a wellbore open hole completion from 272.8 to 290.6 mbsf (Unit 4 sand sub-units #1 to 18 and interbedded mud sub-units of CASE 1, **Figure 4**).

The gas hydrate decomposition is induced by depressurization using a constant pressure of 3.0 MPa at a location just above the top of Unit 4. With the assumed hydrostatic pressure of 28.55 MPa at the top of Unit 4 (which is the top of the main gas hydrate reservoir section), the simulated pressure reduction to 3.0 MPa would represent an 89.5% pressure decrease relative to the expected hydrostatic pressure at the top of the gas hydrate reservoir section.

4. Simulation Cases

CASE 1 was designed to capture a detailed, multi-layered input model based on log data. CASE H tests models of even greater vertical detail and heterogeneity. In the base version of both CASE 1 and CASE H, $K_{ieff,w}$ is 10 mD for the primary reservoir quality sands. These primary cases set intrinsic permeability reduction due to pore compaction using $\gamma = 4.6$ which equates to modest permeability reduction during production. Two alternative simulations were conducted for both CASE H and CASE 1 to assess uncertainty in these parameters. CASE 1b and CASE Hb evaluate the effect of low $K_{ieff,w}$ (0.1 mD) which reflects values historically obtained from NMR logs and MDT (Modular Formation Dynamics Tester) tests, both offshore India and elsewhere (Dai et al., 2017). CASE 1x and CASE Hx evaluate the response assuming high permeability reduction using $\gamma = 17.2$. The analogous cases for CASE 2 (CASE 2b and CASE 2x) are also considered (**Table 6**).

Table 6. Flow simulation cases conducted for Site NGHP-02-16 (Area-B)

CASE	K_{int}, mD sands	$K_{ieff,w}$, mD sands	S_{gh} (%) sands	S_{wf} (%)/S_{wb} (%) sands	γ	Completion
CASE H	Var.	10	Var.	Var.	4.6	GH only
CASE Hb	Var.	0.1	Var.	Var.	4.6	GH only
CASE Hx	Var.	10	Var.	Var.	17.2	GH only
CASE 1	1000	10	80%	10%/10%	4.6	GH only
CASE 1b	1000	0.1	80%	10%/10%	4.6	GH only
CASE 1x	1000	10	80%	10%/10%	17.2	GH only
CASE 2	1000	10	80%	10%/10%	4.6	Open to Aquifer
CASE 2b	1000	0.1	80%	10%/10%	4.6	Open to Aquifer
CASE 2x	1000	10	80%	10%/10%	17.2	Open to Aquifer

In all cases, the reservoir properties are unchanged laterally from the well bore to the reservoir boundary at 500 m. Vertically, CASES 1 and 2 apply the same set of parameters to all gas hydrate bearing sands; whereas CASE H allows for vertical variation in the saturation parameters within sand units (**Figure 5**). We consider CASE H as the base case and the one that should be the primary focus of well test planning activities.

5. Results and Discussion

5.1. Short-term predictions

Figure 10 shows gas production rates and cumulative gas volumes produced for CASES H, Hb, and Hx for 90 days of depressurization. Most notably, CASE H predicts immediate onset of gas production upon initiation of depressurization with rates reaching their peak of 37,000 m^3/day in two days. Subsequently, the rates decrease to about 20,000 m^3/day by day 18 and then slowly increase to 28,000 m^3/day by day 90. These rates are similar with those measured at the Nankai Trough production test (20,000 to 30,000 m^3/day) (Konno et al., 2017).

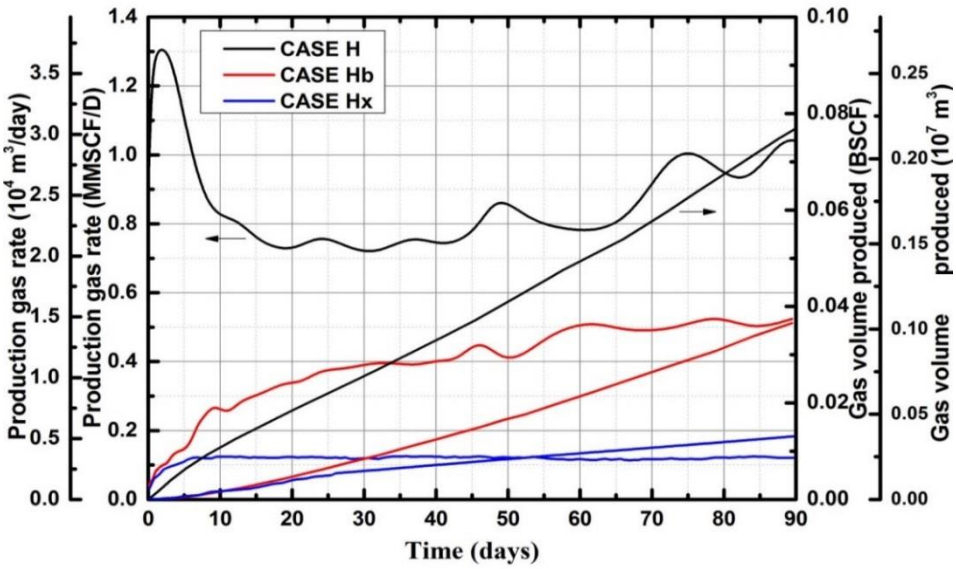

Figure 10. Cumulative production gas volumes and gas rates for 90 days for CASE H, CASE Hb, and CASE Hx.

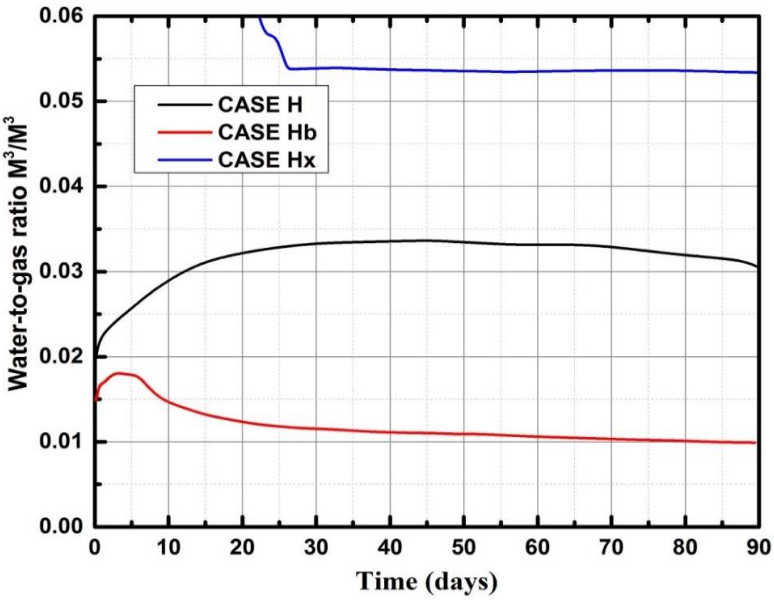

Figure 11. Water to gas ratio for CASE H, CASE Hb, and CASE Hx.

For CASE Hb with $K_{ieff,w}$ = 0.1 mD, the rates are roughly half those of CASE H over 90 days. That indicates a strong sensitivity of the gas production rates on $K_{ieff,w}$ and emphasizes the importance of core and log permeability measurements to estimate variability of $K_{ieff,w}$ for a specific gas hydrate accumulation. In CASE Hx, the effect of the high γ parameter on the gas production rate causes more than eight times decrease relative to CASE H. This strong effect is a consequence of the large depressurization (~25 MPa of pressure drawdown) imposed on this deep reservoir to achieve a maximum driving force, ΔP (pressure difference between the initial reservoir pressure and the well bottom hole pressure set at 3.0 MPa) without possible ice formation. Such large pore pressure decreases cause significant effective stress increases, with the consequent pore space compaction, and reduction of intrinsic permeability (**Figure 8**). Sensitivity analysis has revealed that for a BHP set at 10 MPa, the short-term production rates are similar for CASE Hx (high γ) and about half that of CASE H. This indicates that for deep gas hydrate reservoirs, the choice of a BHP value can be viewed as a balance between maximizing ΔP (the pressure gradient between BHP and a dissociation interface) and reducing intrinsic permeability due to effective stress increase (the pathways for collecting the produced methane). The practical implication of employing mild

depressurization at the beginning of gas production could be also result in a lower likelihood of particle detachment and excess sand production. The simulations reported by Uchida et al. (this issue) indicate increased sand production along the sand – mud boundaries within producing sub-units in comparison with homogeneous gas hydrate-bearing sediment. The greater sand migration is expected because of shearing deformation and greater pressure gradient along the sand – mud sub-units.

Figure 11 shows that water-to-gas production ratios remain stable throughout the 90 day production at approximately 0.033, 0.010, 0.053 for CASE H, CASE Hb, and CASE Hx respectively. At the Nankai Trough site, the simulations predict the water-to-gas ratio to be about 0.010 at day 6, which is in agreement with measured gas and water rates (Konno et al., 2017). For later times the simulations of the Nankai Tough reservoir indicate that the ratio is kept at the slightly lower value, close to 0.007.

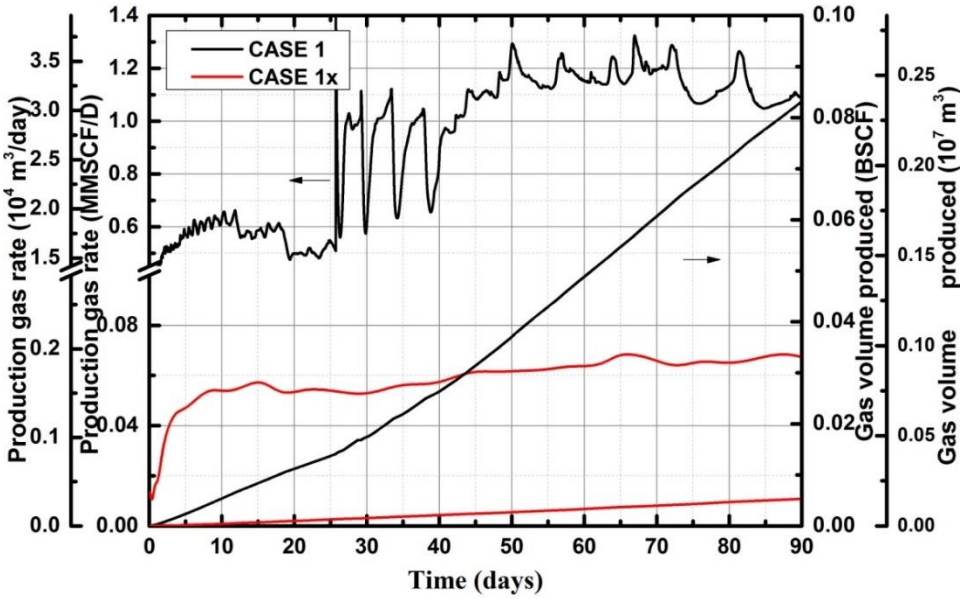

Figure 12. Cumulative production gas volumes and gas rates for 90 days for CASE 1 (black line) and CASE 1x (red line).

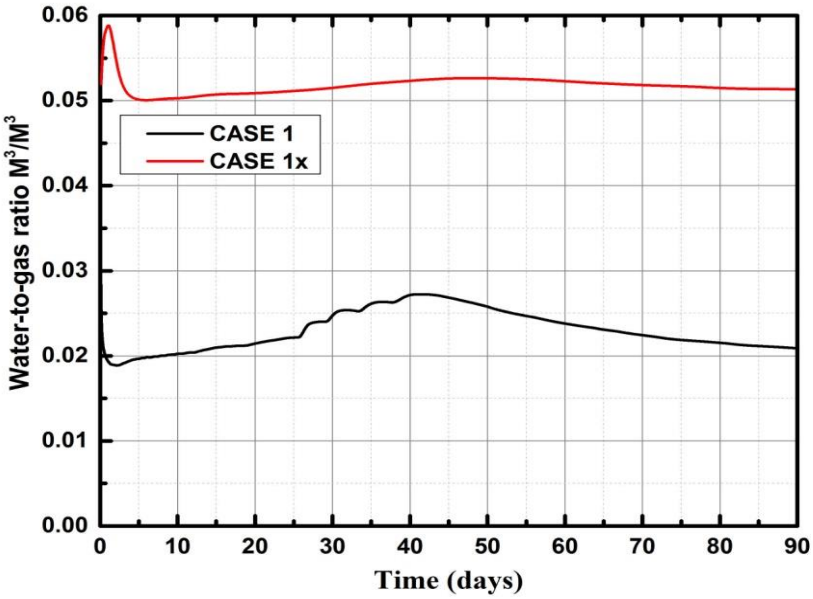

Figure 13. Water to gas ratio for CASE 1 and CASE 1x.

Given that the volumetric ratio of water-to-gas volumes released after decomposition of 1 m^3 of methane hydrate (at the hydration number equal to 6.0 and standard P/T conditions) is around 0.005, the stabilization of the ratio of produced water-to-gas volumes at the Nankai Trough site suggests that heat transfer supporting the decomposition reaction becomes a dominant factor controlling the production rates.

CASE 1 predicts gas production with rates generally growing from 15,000 to 30,000 m^3/day through day 50 (**Figure 12**). CASE 1 and CASE H both respond to depressurization with similar maximum gas rates and cumulative gas volumes. They differ however in that CASE H predicts an initial high production rate, followed by a rate reduction and then steadily increasing production after day 15. CASE 1 however, shows steady production growth through day 60 after which the rate appears to plateau. **Figure 13** displays water-to-gas ratios for CASE 1 and CASE 1x showing that the former provides better performance over 90 days of depressurization. The ratio remains stable throughout the 90 day production at approximately 0.025 and 0.052 for CASE 1 and 1x, respectively. The averaged ratio for CASE 1 is comparable to the ratio estimated for CASE H (0.033).

Table 7 summarizes the maximum gas production rates during 60 days of depressurization, cumulative gas volume, and water volumes produced from all flow simulation cases reported at 60 days. **Table 8** collects information on gas and water rates and gas and water volumes at 30, 60, 90 days for CASE H, CASE 1, and CASE 2. As expected, the various flow simulations reveal a high sensitivity to the values of both K_{ieff} and γ, which profoundly affect flow in the reservoir. Notably, CASEs 1b and 2b (with $K_{ieff,w}$ = 0.1 mD) and CASEs 1x and 2x (with $K_{ieff,w}$ = 10 mD and γ = 17.2) all result in low production given the input data and assumptions.

Table 7. Short-term predictions of production gas rates, cumulative gas volumes and water volumes produced for the simulation cases together with generalized results.

CASE	Max gas rate (m^3/d)	Cum. gas volume (m^3) at 60 days	Water volume (m^3) at 60 days	Comment
CASE H	37,020	1,456,200	44,300	Detailed geologic input model
CASE Hb	15,190	628,300	6,620	Low production (low $K_{ieff,w}$)
CASE Hx	3,494	26,978	14,437	Low production (low $K_{ieff,w}$ due to high γ)
CASE 1	39,240	1,375,500	32,700	Conservative geologic model
CASE 1b	Negligible production			Negligible production (low $K_{ieff,w}$)
CASE 1x	1,960	90,050	5,120	Low production (low $K_{ieff,w}$ due to high γ)
CASE 2	28,706	1,211,600	59,100	Results assume confined aquifer.
CASE 2b	2,440	91,959	41,202	Low production (low $K_{ieff,w}$)
CASE 2x	2,910	131,107	20,361	Low production (low $K_{ieff,w}$ due to high γ)

Table 8. Daily average rates of gas and water produced, along with cumulative volumes short-term predicted at 30, 60, and 90 days for CASE H, CASE 1, and CASE 2.

	Gas			**Water**		
	30 days	**60 days**	**90 days**	**30 days**	**60 days**	**90 days**
			CASE H			
Rate (m^3/d)	20,400	22,000	29,100	715	741	726
Volume (m^3)	759,600	1,456,200	2,175,400	25,300	44,300	67,100
			CASE 1			
Rate (m^3/d)	17,200	32,500	30,700	934	565	512
Volume (m^3)	490,900	1,375,500	2,341,700	12,100	32,700	48,900
			CASE 2			
Rate (m^3/d)	19,300	23,100	28,700	995	960	914
Volume (m^3)	566,000	1,211,600	1,982,100	29,700	59,100	87,300

CASE 2 is an alternative case of CASE 1 (using the same vertical geologic characterization and model structure) which explores the potential production if the well completion allows for water withdrawal from the underlying water-bearing sands, just below the deepest gas hydrate-bearing sand in sub-unit #18 (**Figure 4**). CASE 2 results in accelerated gas production from the basal gas hydrate-bearing sand due to very effective (rapid and widespread) reduction of pressure within the subjacent aquifer. This pressure

reduction is enabled both by the high $K_{ieff,w}$ of the water bearing units (1,000 mD) as well as the assumption that water does not flow into the water-bearing zone laterally from beyond the modeling domain (i.e., across the faults marking the boundaries of Site NGHP-02-16 fault block). Based on the evaluation of the seismic data from Site NGHP-02-16, such lateral confinement is certainly possible (Collett et al., this issue). However, this confinement is not assured, and should it not be present, a scientific production test at the site would likely fail due to excessive water input that would strongly hamper effective depressurization. To ensure that maximum scientific insight is obtained from any Site NGHP-02-16 test, a completion such as that modeled in CASE 2 is not recommended.

5.2. Long-term predictions

Figures 14 and **15** show results of production simulations for CASE H and CASE 1 for 5 and 20 years, respectively. In both cases, the predictions are based on the same mesh and reservoir parameters (**Tables 4** and **5**). **Table 9** summarizes the daily average rates of gas and water produced, along with predicted volumes at selected time points for these two cases. The CASE H results were limited to 5 years because of convergence issues.

The predicted long-term production rates for CASE 1 and CASE H display short-term fluctuations within the first five years (**Figure 14**). In CASE 1, rates range from approximately 3,100 to 42,500 m^3/day, while the rates for CASE H range more narrowly from 17,000 to 45,300 m^3/day. CASE 1 rates drop after approximately 3 years of production and reach the minimum at around 4.5 years. After 5 years, the CASE 1 rates show two major peaks at around 10 and 18 years. The water-to-gas ratio is lower in CASE 1 than in CASE H (**Figure 15**). The greater water-to-gas ratio in CASE H is attributed to larger initial free water volumes (5-20% *vs* 10% of pore space) and lesser gas hydrate reformation hindering reservoir performance (due to reasons discussed below).

Figures 16 and **17** display gas hydrate saturation, pressure and temperature distributions within the reservoir model at selected time points. In both CASE 1 and CASE H, the gas hydrate distribution

indicates that gas hydrate dissociation occurs along horizontal interfaces between the gas hydrate sub-units and adjacent mud layers. Those dissociation interfaces develop at the beginning of the simulations as soon as depressurization is induced. The high-permeability intervals formed at the upper and lower boundaries of each reservoir sub-unit create preferential flow pathways towards the wellbore. The interfaces of gas hydrate decomposition are maintained throughout the entire production period and steadily converge toward the vertical mid-point of each sub-unit. The abundance of such horizontal interfaces in interbedded deposits renders these surfaces the primary sources of gas production, as opposed to vertical dissociation fronts within individual sub-units (**Figure 18**).

It should be noted that lateral homogeneity assumed in CASE 1 and CASE H is an approximation implemented due to a current lack of rigorous field data available to shed light into key reservoir property heterogeneity away from the wellbore. Geophysical data for the site (Shukla et al., this issue) confirm that the reservoirs show no structural or stratigraphic complications that would obstruct flow within 500 m from the selected well site. Given that deep-water unconfined deposits tend to have a high degree of lateral continuity (Collett et al., this issue), long-term predictions reported here probably provide close estimates to more elaborate models. Nonetheless, the refinement of long-term production potential is needed using a 3-D reservoir model with lateral heterogeneity to make an accurate prognosis of production viability of Site NGHP-02-16.

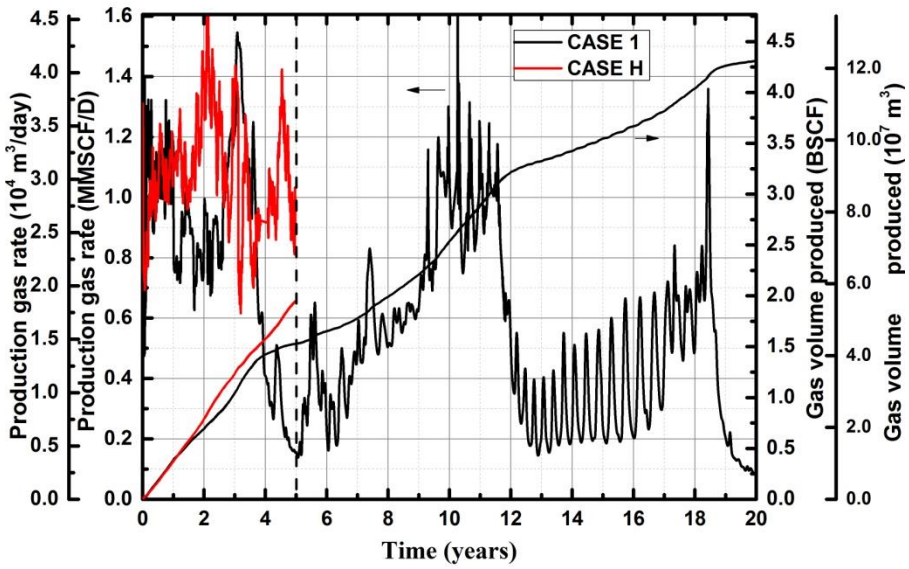

Figure 14. Cumulative production gas volumes (red line) and gas rates (black lines) for CASE 1 and CASE H.

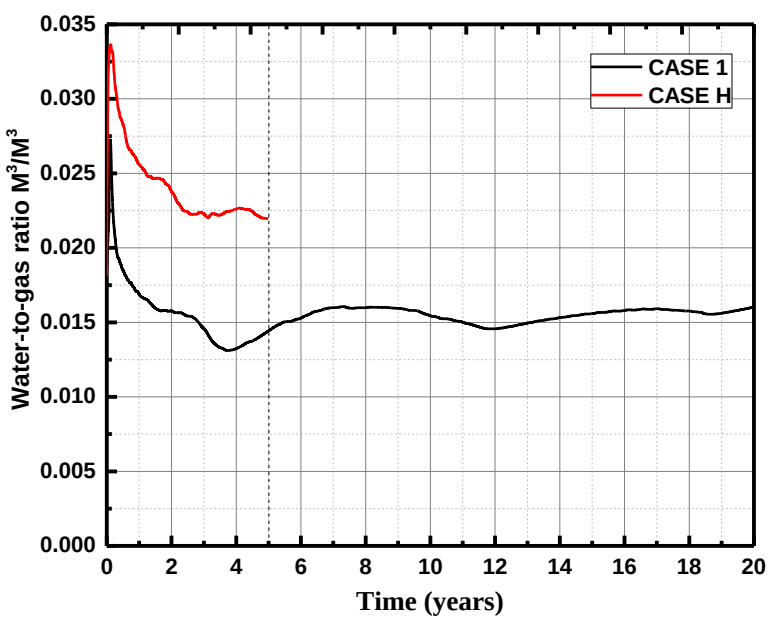

Figure 15. Water to gas ratio for CASE 1 and CASE H.

Table 9. Daily average rates of gas and water produced, along with cumulative volumes predicted at 0.5, 1, 2, and 5 years for CASE H and 0.5, 1, 2, 5, 10, and 20 years for CASE 1.

	0.5 year	1 year	2 years	5 years	10 years	20 years
			CASE H			
Gas Rate (m^3/d)	27,900	31,500	39,600	29,700	-	-
Gas Volume (m^3)	4,717,00	10,518,00	22,251,000	54,833,000	-	-
Water Rate (m^3/d)	733	729	695	533	-	-
Water Volume (m^3)	134,700	269,100	528,900	1,205,000	-	-
			CASE 1			
Gas Rate (m^3/d)	29,400	32,900	28,500	4,700	26,700	2,228
Gas Volume (m^3)	4,986,000	10,761,000	19,629,000	42,965,000	72,499,000	121,224,000
Water Rate (m^3/d)	494	544	357	258	374	181
Water Volume (m^3)	92,400	181,800	309,600	616,000	1,116,000	1,949,000

The key feature noticed in CASE 1 is that the gas production rate displays irregular rapid rises and drops (**Figure 14**). The feature can be correlated with intense gas hydrate dissociation focused on specific gas hydrate sub-units such as #2, #13 and #17 in the first 10 years (**Figure 17**). The faster decomposition of #2, and #17 can be attributed to the proximity of the overburden and underburden, which provide large sources of sensible heat to maintain the gas hydrate dissociation reaction. Such behavior is similar to previous predictions showing preferential decomposition at the tops and bottoms of gas hydrate-bearing layers in response to depressurization. The reason for the fast dissociation of #13 is unclear, but is likely connected to sensible heat availability in the surrounding layers to support the decomposition reaction.

One observation clearly noticed for CASE 1 is elevated gas hydrate saturation due to secondary gas hydrate reformation approximately 5 to 100 m from the wellbore. The phenomenon is interpreted to relate to conversion of dissolved methane from formation water into the gas hydrate phase due to reduced temperature and reduced methane solubility (Lu et al., 2008; Servio and Englezos, 2001) as methane-rich pore fluid from beyond the gas hydrate dissociation front migrates toward the wellbore. Because of this additional gas hydrate reformation, local gas hydrate saturations can reach up close to 90% (from initial values of 80%) near the wellbore, which make those zones virtually impermeable for further flow (**Figure 17**). Given that irreducible water saturation in the reservoir is set at 10%, reaching S_{gh} = 90% means practically no flow occurs within the corresponding grid blocks. At the same time, the high-permeability

zones at the horizontal interfaces remain capable of transmitting fluids. Gas hydrate dissociates in the areas behind the secondary gas hydrate reformation zone because of availability of free water and continuous exposure to the pressure drop.

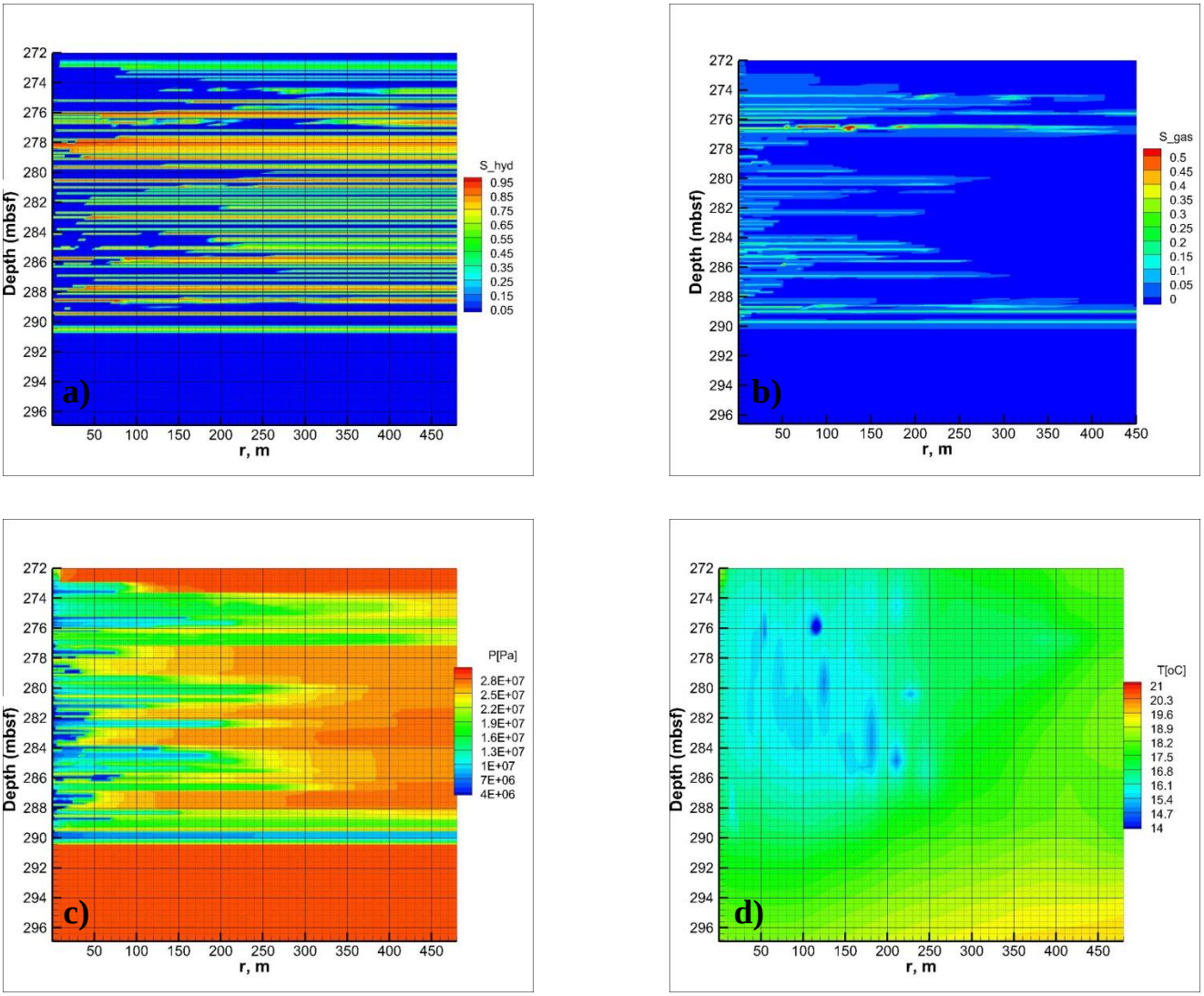

Figure 16. Gas hydrate saturation (**a**), gas saturation (**b**), pressure (**c**), and temperature (**d**) distributions in the Site NGHP-02-16 reservoir after 2 years of production for CASE H.

As time progresses, gas hydrate dissociation along the horizontal interfaces between gas hydrate-bearing sands and muds can create gas hydrate-free areas within some gas hydrate-bearing sub-units that are separated from the wellbore by areas where gas hydrate with high saturations persists (**Figure 17**). This

phenomenon, which may not be representative of a process that would actually occur in a production test, is referred as vertical "splitting" in gas hydrate saturation distribution as shown in **Figure 17**, and may largely be an artifact of the homogeneity imposed on the gas hydrate-bearing layers in CASE 1. CASE H, for example, uses thinner gas hydrate sub-units with varied gas hydrate saturation and permeabilities, and shows less gas hydrate reformation and "splitting" (although it is observed in the thicker layers, **Figure 16**). The heterogeneity incorporated into gas hydrate saturations and permeability description of the gas hydrate-bearing sands also induces faster development of the horizontal interfaces.

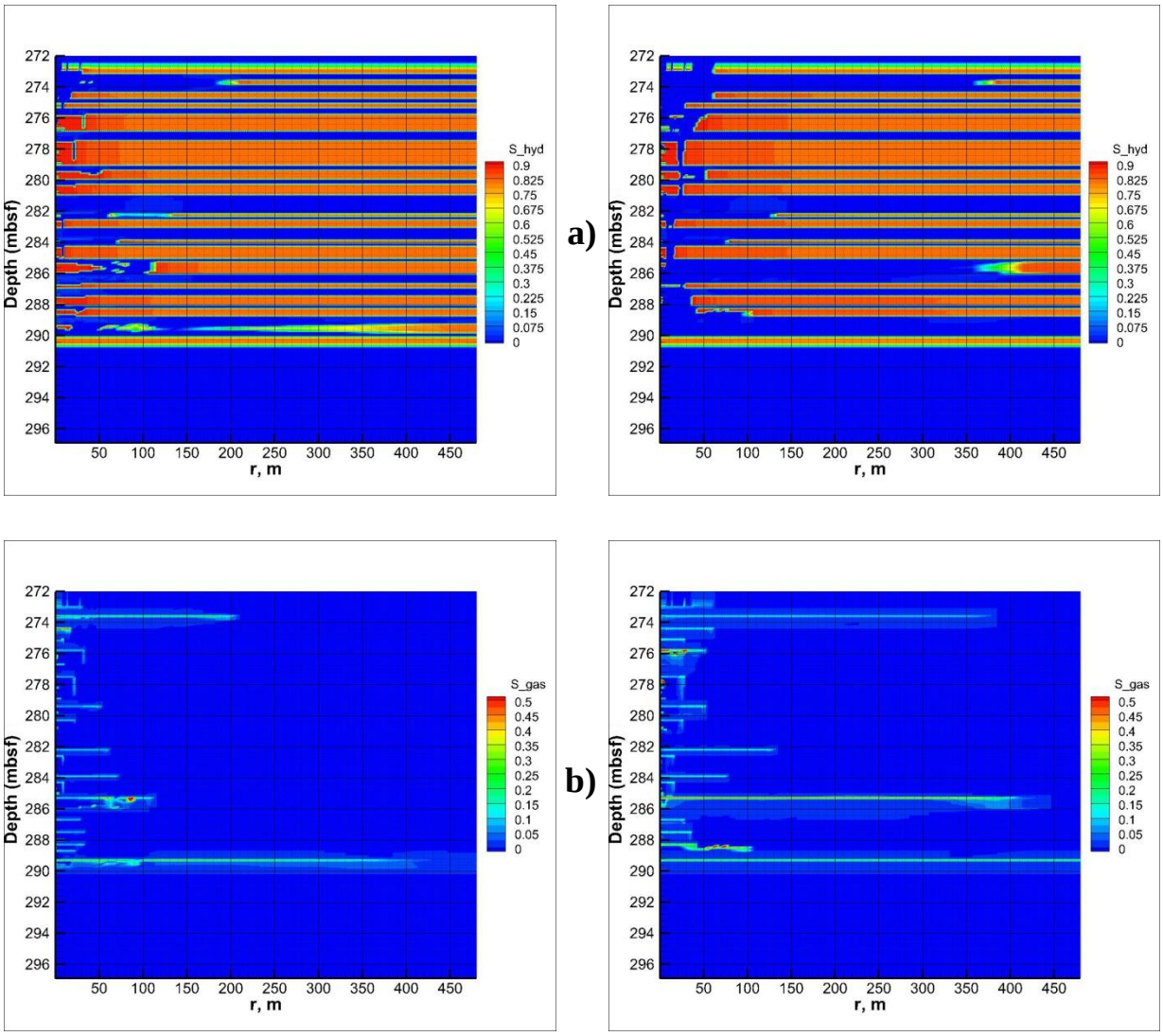

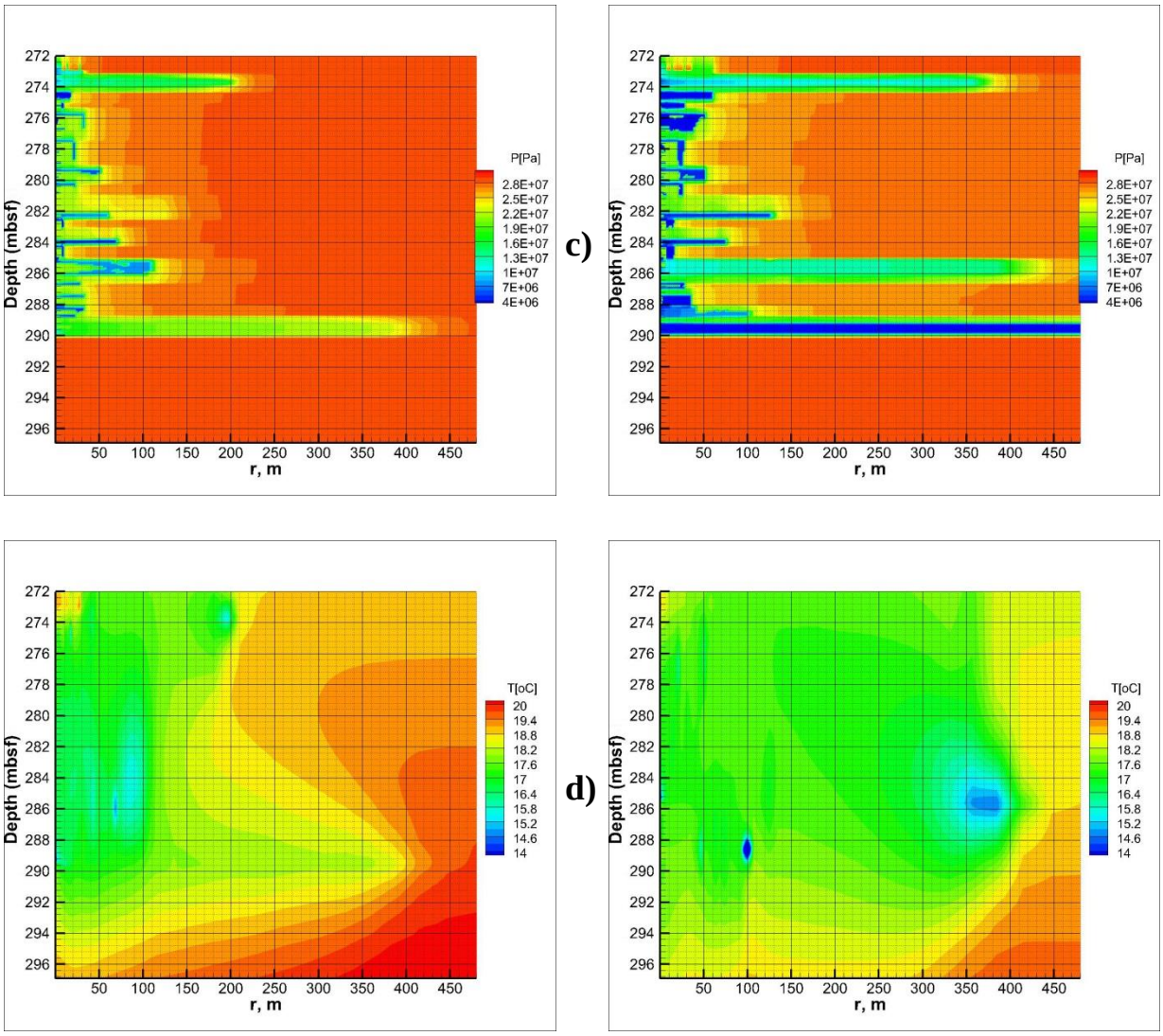

Figure 17. Gas hydrate saturation (**a**), gas saturation (**b**), pressure (**c**), and temperature (**d**) distributions in the reservoir after 2 years (left column) and 10 years (right column) of production for CASE 1.

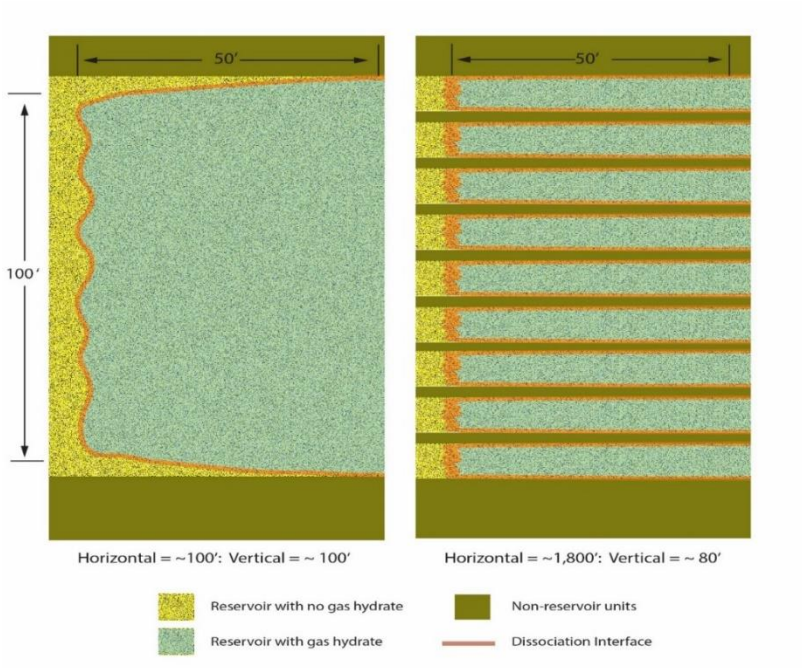

Figure 18. Schematic showing the dominance of horizontal dissociation interfaces (shown in orange) in thinly-bedded reservoirs.

In summary, the additional heterogeneity of the Case H gas hydrate distribution causes slight modifications in simulated reservoir behavior over the first five years, including the removal (or delay) of a large production rate decrease that occurs at ~ year 3 in CASE 1 due to gas hydrate reformation. The Site NGHP-02-16 reservoir is noted for its substantial complexity, particularly the development of vertical and horizontal dissociation interfaces. These interfaces represent areas of large variation in reservoir petrographic parameters over very short distances. The results of the modeling are the best that can be accomplished at this time, but may reflect limitations on current modeling capabilities. We do truly need better reservoir data like comprehensive geologic information on reservoir heterogeneity, structural and lithologic complexity, hydraulic isolation, geomechanical effects on porosity/permeability, permeability anisotropy, mineralogy and grain size analysis, thermal conductivity of representative core samples, and more actual production test data first to both refine our assignment of key parameters and to provide calibration data to allow differentiation of likely reservoir response from potential numerical artefacts related to model set-up and performance.

6. Conclusions

Multiple simulation cases of gas production were conducted to investigate reservoir flow in response to depressurization at Site NGHP-02-16. Two primary cases are modeled, CASE 1 uses a generalized geologic input model designed to capture multi-layer interbedded input based on log data. CASE H uses a detailed geologic model allowing for modest vertical gas hydrate saturation and intrinsic permeability heterogeneity for target gas hydrate-bearing sands. Both simulations are fully consistent with the available well log and core information gathered during NGHP-02 and subsequent analyses. The results of these cases, and a number of alternative cases that reflect uncertainty in the initial permeability (cases 'b") and reservoir response to effective stress change (cases "x") provide a range of potential gas and water flow rates. In both CASE 1 and CASE H, peak gas production rates of ~30,000 m^3/day are predicted for the initial 90 days of depressurization. Peak rates as low as ~1800 m^3/day were generated for the more pessimistic cases.

Our modeling indicates that dissociation is initially and preferentially localized at horizontal interfaces between gas hydrate-bearing sands and non-gas hydrate-bearing muds. In CASE 1, the evolution of hydrate dissociation in the lateral direction is hindered by the secondary formation of gas hydrate in the reservoir at or beyond the dissociation front. However, in CASE H, increasing the fidelity of the geologic input model to natural conditions by incorporating thinner units with greater heterogeneity appears to diminish the apparent formation of secondary gas hydrate. Over a 90-day simulation, the two cases result in similar production rates and volumes, although CASE H shows evidence of greater production sustainability over longer time frames (~30,000 m^3/d over 5 years). CASE 1 demonstrates fluctuations of production rates ranging from ~3,000 to ~45,000 m^3/d over 20 years that can be related to the secondary gas hydrate formation.

The key findings of this study are summarized below:

- The proximity of the BGHSZ and high initial temperature in the reservoir make it an attractive target for depressurization to induce gas production, and this is supported by the results of the numerical simulations;
- The hydraulic isolation through well design of the underlying (assumed confined) aquifer is critical, since under similar reservoir performance (CASE 1 and CASE 2), the case with open communication with the aquifer (CASE 2) is predicted to produce nearly double the volume of water, imposing a large load on the lifting system;
- The interbedded nature of the reservoir defines the uniqueness of the dissociation interface shape that is dominated by horizontal interfaces developing along the boundaries between the gas hydrate-bearing sand and mud sub-units;
- The thinly-interbedded architecture of the reservoir emphasizes the importance of implementing heterogeneity into the CASE H description of key reservoir properties like gas hydrate saturation and permeability. CASE H is less prone to gas hydrate reformation and demonstrates more steady production rates over 5 years of depressurization when compared to CASE 1;
- To capture the uncertainty of *in situ* permeability, the simulation cases with 0.1 and 10 mD of initial effective horizontal permeability were considered. The results reveal almost an order of magnitude decrease in the cumulative volume produced (CASE H and CASE Hb) for the case with low permeability value (CASE Hb, predicted after 60 days of production);
- As revealed by experimental studies (Yoneda et al. this issue-c; Dai et al., this issue), the pore space is prone to large compaction under high effective stresses that greatly impacts (reduces) absolute permeability. The cases using medium and high sensitivity of absolute permeability to compaction (CASE H and CASE Hx, respectively) show about two orders of magnitude difference (predicted after 60 days of production). That suggests that a final bottom hole pressure should be carefully chosen, accounting for reduction of intrinsic permeability with increase of effective confining stress.

The results of the numerical simulations indicate that the Site NGHP-02-16 reservoir will respond to an extended duration of depressurization in a fashion that will yield important insights into the reservoir potential of gas hydrates in India and worldwide. While additional laboratory study and numerical simulation are clearly warranted, those studies likely cannot progress toward a fuller understanding of gas hydrate reservoir behavior without additional closely monitored field production experiments. The proposed field experiments, and the careful observation of gas and water flow rates as well as sand mobilization and subsidence, provide the only means to better constrain the uncertainties associated with gas hydrate production potential. Major challenges are associated with 1) the nature of reservoir permeability and how that permeability evolves during dissociation and compaction; 2) the flow of heat within the producing reservoir and the ability to sustain depressurization over extended areas and timeframes; and 3) the geomechanical response of the reservoir to depressurization and gas/water withdrawal is particularly important for marine gas hydrate deposits sandwiched between unconsolidated muddy units. The results of this work highlight the importance of honoring geologic information, such as stratigraphic setting, facies types, and depositional environments in a reservoir model in order to properly account for various phenomena arising during gas production. The development of horizontal dissociation interfaces and enhanced sand migration are the consequences of the detailed geological information incorporated in the Site NGHP-02-16 reservoir model. The interbedded architecture of this gas hydrate reservoir is reminiscent of the gas hydrate accumulation at the Green Canyon 955 site in the Gulf of Mexico (Haines et al., 2017). Future numerical characterization of that deposit using either logging information or core sampling should focus on such fine details in order to enable more accurate reservoir modeling.

Acknowledgment

The authors are thankful to Dr. William Waite of the U.S. Geological Survey for fruitful discussions and providing valuable comments to this paper. This technical effort was performed in support of the National Energy Technology Laboratory's ongoing research under the RES contract DE-FE0004000. The authors

are thankful to the Ministry of Petroleum & Natural Gas within the Government of India, Oil and Natural Gas Corporation Limited (ONGC), Directorate General of Hydrocarbons (DGH), Oil India Ltd, GAIL (India) Ltd, Indian Oil Corporation Ltd and all other NGHP partner organizations for providing the opportunity to contribute to the NGHP-02 Expedition and this special issue of the Journal of Marine and Petroleum Geology. The technical and science support from the Japan Agency for Marine-Earth Science and Technology, the United States Geological Surveyand Department of Energy, the Japanese National Institute of Advanced Industrial Science and Technology, Geotek Coring and Schlumberger is gratefully acknowledged.

Disclaimer

This project was funded by the Department of Energy, National Energy Technology Laboratory, an agency of the United States Government, through a support contract with AECOM. Neither the United States Government nor any agency thereof, nor any of their employees, nor AECOM, nor any of their employees, makes any warranty, expressed or implied, or assumes any legal liability or responsibility for the accuracy, completeness, or usefulness of any information, apparatus, product, or process disclosed, or represents that its use would not infringe privately owned rights. Reference herein to any specific commercial product, process, or service by trade name, trademark, manufacturer, or otherwise, does not necessarily constitute or imply its endorsement, recommendation, or favoring by the United States Government or any agency thereof. Any use of trade, firm or product name is for descriptive purposes only and does not imply endorsement by the U.S. Government. The views and opinions of authors expressed herein do not necessarily state or reflect those of the United States Government or any agency thereof.

References:

Ajayi, T., Anderson, B. J., Seol, Y., Boswell, R., Myshakin, E. M. 2018. Key aspects of numerical analysis of gas hydrate reservoir performance: Alaska North Slope Prudhoe Bay Unit "L-Pad" hydrate accumulation. Journal of Natural Gas Science and Engineering, **51**, 37–43.

Anand, J., Somerton, W.H., Gomaa, E. 1973. Predicting thermal conductivities of formations from other known properties, SPE Journal, **13** (5), 267-273.

Anderson, B.J., Kurihara, M., White, M.D., Moridis, G.J., Wilson, S.J., Pooladi-Darvish, M., Gaddipati, M., Masuda, Y., Collett, T.S., Hunter, R.B., Narita, H., Rose, K., Boswell, R. 2011. Regional long-term production modeling from a single well test, Mount Elbert Gas Hydrate Stratigraphic Test Well, Alaska North Slope. Journal of Marine and Petroleum Geology, **28** (2), 493-501.

Bolton, M. D., Nakata, Y., Cheng, Y. P. 2008. Micro- and macro-mechanical behavior of DEM crushable materials. Geotechnique, **58** (6), 471-480.

Boswell, R., Myshakin, E., Moridis, G., Konno, Y., Collett, T., Reagan, M., Ajayi, T., Seol, Y. this issue-a, India National Gas Hydrate Program Expedition 02 summary of scientific results: Numerical simulation of reservoir response to depressurization. Marine and Petroleum Geology, https://doi.org/10.1016/j.marpetgeo.2018.09.026

Boswell, R., Yoneda, J., Waite, W. this issue-b. India National Gas Hydrate Expedition 02 summary of scientific results: Evaluation of natural gas hydrate-bearing pressure cores. Marine and Petroleum Geology, https://doi.org/10.1016/j.marpetgeo.2018.10.020

Boswell, R., Collett, T., Myshakin, E., Ajayi, T., Seol, Y. 2017. The increasingly complex challenge of gas hydrate reservoir simulation, Proceedings, 9th International Conference on Gas Hydrates, Denver, CO, June 25-30, 2017.

Boswell, R., Shipp, C., Riechel, T., Shelander, D., Saeki, T., Frye, M., Shedd, W., Collett, T., McConnell, D. 2016. Prospecting for marine gas hydrate resources. Interpretation, **4** (1), SA13-SA24.

Boswell, R., Yamamoto, K., Lee, S-R., Collett, T., Kumar, P., Dallimore, S. 2014. Methane Hydrates. In: Letcher, T., ed., Future Energy, 2nd Edition, Elsevier, 159-178.

Boswell, R., Shelander, D., Lee, M., Latham, T., Collett, T., Guerin, G., Moridis, G., Reagan, M., Goldberg, D. 2009. Occurrence of gas hydrate in Oligocene Frio sand: Alaminos Canyon Block 818: Northern Gulf of Mexico. Marine and Petroleum Geology, **26** (8), 1499-1512.

Brooks, R. H., and A. T. Corey. 1964. Hydraulic properties of porous media, Hydrol. Pap. 3, Civ. Eng. Dep., Colo. State Univ., Fort Collins, CO.

Clauser, C., Huenges, E., 1995. Thermal conductivity of rocks and minerals. Rock physics & phase relations: A handbook of physical constants, p. 105-126.

Collett, T., Johnson, A., Knapp, C., Boswell, R. 2009. Natural Gas Hydrates – A Review: in Collett, T., Johnson, A., Knapp, C., Boswell, R., eds, Natural Gas Hydrates: Energy Resource and Associated Geologic Hazards; AAPG Memoir **89**, Ch. 1; 146-220.

Collett, T., Kumar, P., Singh, S., Chopra, K., et al. this issue. India National Gas Hydrate Program Expedition 02 – Scientific Results. Marine and Petroleum Geology.

Collett, T., Boswell, R., Cochran, J., Kumar, P., Lall, M., Mazumdar, A., Ramana, M., Ramprasad, T., Riedel, M., Sain, K., Sathe, A., Vishwanath, K. 2014. Geologic implications of gas hydrates in the offshore of India: Results of the National Gas Hydrate Program Expedition 01. Marine and Petroleum Geology **58**, 1-28.

Dai, S., Kim, J., Xu, Y., Waite, W., Jang, J., Yoneda, J., Collett, T., Kumar, P. this issue. Permeability anisotropy and relative permeability in sediments from the National Gas Hydrate Program Expedition 02, offshore India. Marine and Petroleum Geology, https://doi.org/10.1016/j.marpetgeo.2018.08.016

Dai, S., Boswell, R., Waite, W., Jang, J., Lee, J., Seol, Y. 2017. What has been learned from pressure cores? Proceedings, 9th International Conference on Gas Hydrates, Denver, CO, June 25-30, 2017.

Dallimore, S. R., Yamamoto, K., Wright, J. F., Bellefleur, G. (Eds.) 2012. Scientific results from the JOGMEC/NRCan/Aurora Mallik 2007-2008 gas hydrate production research well program, Mackenzie Delta, Northwest Territories, Canada; Geological Survey of Canada, Bulletin 601, 35-51.

Dallimore, S.R., and Collett, T. S. (Eds.) 2005. Scientific results from the Mallik 2002 gas hydrate production well program, Mackenzie Delta, Northwest Territories, Geological Survey of Canada Bulletin, 585.

Dickens, G.R., Quinby-Hunt, M.S., 1997. Methane hydrate stability in pore water: A simple theoretical approach for geophysical applications. JGR: Solid Earth, 102, 773–783.

Friend D., Ely, J. F. 1989. Thermophysical properties of methane, Journal of Physical and Chemical Reference Data, **18** (2), 583-638.

Flemings, P., Boswell, R., Collett, T., Cook, A., Divins, D., Frye, M., Guerin, G., Goldberg, D., Malinverno, A., Meazell, K., Morrison, J., Pettigrew, T., Phillips, S., Santra, M., Sawyer, D., Shedd, W., Thomas, C., You, K. 2017. GOM2: prospecting, drilling, and sampling coarse-grained hydrate reservoirs in the deep-water Gulf of Mexico. Proceedings, 9th International Conference in Gas Hydrates, Denver, CO, June 24-29, 2017.

Fujii, T., Namikawa, T., Okui, T., Kawasaki, M., Ochiai, K., Nakamizu, M., Nishimura, M., Takano, O., Tsuji, Y. 2009. Methane hydrate occurrence and saturation confirmed from core samples, eastern Nankai Trough, Japan. AAPG Memoir, **89**, 385-400.

Gaddipati, M., and Anderson, B.J. 2012. 3D Reservoir modeling of depressurization-induced gas production from gas hydrate reservoirs at the Walker Ridge site, Northern Gulf of Mexico. OTC-23582-MS. In: Offshore Technology Conference, Houston, Texas, 30 April -3 May 2012.

Haines, S. S., Hart, P. E., Collett, T. S., Shedd, W., Frye, M., Weimer, P., Boswell, R. 2017. High-resolution seismic characterization of the gas and gas hydrate system at Green Canyon 955, Gulf of Mexico, USA. Marine and Petroleum Geology, **82**, 220-237.

Hunter, R., Collett, T., Boswell, R., Anderson, B., Digert, S., Pospisil, G., Baker, R., Weeks, L. 2011. Mount Elbert gas hydrate stratigraphic test well, Alaska North Slope: Overview of scientific and technical program. Marine and Petroleum Geology, **28** (2), 295-310.

Jang, J., Waite, W. F., Stern, L., Collett, T., Kumar, P. this issue-a. Physical property characteristics of gas hydrate-bearing reservoir and associated seal sediments collected during NGHP-02 in the Krishna-Godavari Basin, in the offshore of India. Marine and Petroleum Geology, https://doi.org/10.1016/j.marpetgeo.2018.09.027

Jang, J., Dai, S., Yoneda, J., Waite, W. F., Stern, L. A., Boze, L.-G., Collett, T. S., Kumar, P. this issue-b. Pressure core analysis of geomechanical and fluid flow properties of seals associated with gas hydrate-bearing reservoir in

the Krishna-Godavari Basin, offshore India. Marine and Petroleum Geology, https://doi.org/10.1016/j.marpetgeo.2018.08.015

Kim, J., Dai, S., Jang, J., Waite, W. F., Collett, T. S., Kumar, P. this issue. Compressibility and particle crushing of Krishna-Godavari Basin sediments from offshore India: Implications for gas production from deep-water gas hydrate deposits. Marine and Petroleum Geology, https://doi.org/10.1016/j.marpetgeo.2018.07.012

Kneafsey, T., Seol, Y., Gupta, A., Tomutsa, L. 2011. Permeability of laboratory-formed methane hydrate-bearing sand: measurements and observations using X-Ray computed tomography. SPE Journal, **16** (1), 78-94.

Konno, Y., Fujii, T., Sato, A., Akamine, K., Naiki, M., Masuda, Y., Yamamoto, K., Nagao, J. 2017. Key findings of the world's first offshore methane hydrate production test off the coast of Japan: toward future commercial production, Energy & Fuels, **31** (3), 2607–2616.

Konno, Y., Yoneda, J., Egawa, K., Ito, T., Jin, Y., Kida, M., Suzuki, K., Fujii, T., Nagao, J. 2015. Permeability of sediment cores from methane hydrate deposit in the eastern Nankai Trough. Marine and Petroleum Geology, **66**, 487-495.

Kowalsky, M.B., and Moridis, G.J. 2007. Comparison of kinetic and equilibrium reaction models in simulating the behavior of gas hydrates in porous media, Journal of Energy Conversion and Management, **48**, 1850-1863.

Kumar, P., Collett, T., Yadav, U., Boswell, R., Cochran, J., Lall, M.., Mazumdar, A., Ramana, M., Ramprasad, T., Riedel, M., Sain, K., Sathe, A., Vishwanath, K. 2014. Geologic implications of gas hydrates in the offshore of India: Krishna-Godavari Basin, Mahanadi Basin, Andaman Sea, and Kerala-Konkan Basin. Marine and Petroleum Geology, **58**, 29-98.

Kumar, P., Collett, T., et al. this issue. India National Gas Hydrate Program Expedition 02 – operational and technical summary. Marine and Petroleum Geology. Marine and Petroleum Geology.

Kurihara, M., Sato, A., Ouchi, H., Narita, H., Masuda, Y. 2008. Prediction of gas productivity from Eastern Nankai Trough methane-hydrate reservoirs. OTC 19382. In: Offshore Technology Conference, Houston, TX, 5-8 May.

Lin, J. S., Uchida, S., Myshakin, E. M., Seol, Y., Rutqvist, J., Boswell, R. this issue. Assessing the geomechanical stability of interbedded hydrate-bearing sediments under gas production by depressurization at Site NGHP-02-16. Marine and Petroleum Geology, https://doi.org/10.1016/j.marpetgeo.2018.08.018

Lu, W., Chou, M., Burruss, R. C. 2008. Determination of methane concentrations in water in equilibrium with sI methane hydrate in the absence of a vapor phase by *in situ* Raman spectroscopy. Geochem. Cosmochem. Acta, **72** (2), 412-422.

Mahabadi, N., Dai, S., Seol, Y., Sup Yun, T., Jang, J. 2016. The water retention curve and relative permeability for gas production from hydrate-bearing sediments: pore-network model simulation. Geochem. Geophys. Geosyst., **17**, 3099–3110.

Maxwell, J. A. 1954. A Treatise on Electricity and Magnetism, Vol. 1, 3rd Ed. New York: Dover, Chapter 9, Article 314.

Midttømme, K., Roaldset, E., Aagaard, P. 1988. Thermal conductivity claystones and mudstones of selected from England. Clay Minerals, **33** (1), 131-145.

Moridis, G. J. 2014. User's manual for the hydrate v1.5 option of Tough+ v1.5: A code for simulation of system behavior in hydrate-bearing geologic media. Earth Sciences Division, Lawrence Berkeley National Laboratory, Berkeley, CA.

Moridis, G.J., J. Kim, Reagan, M. T., Kim, S.-J. 2013. Feasibility of gas production from a gas hydrate accumulation at the UBGH2-6 site of the Ulleung basin in the Korean East Sea. Journal of Petroleum Science and Engineering, **108**, 180-210.

Moridis, G., Collett, T., Boswell, R., Kurihara, M., Reagan, M., Sloan, D., Koh, C. 2009. Toward production from gas hydrates: current status, assessment of resources, and simulation-based evaluation of technology and potential. SPE Reservoir Evaluation and Engineering, **12** (5), 745-771.

Moridis, G. J., Collett, T., Dallimore S., Satoh T., Hancock S.; Weatherhill, B. 2004. Numerical studies of gas production from several methane hydrate zones at the Mallik site, Mackenzie Delta, Canada. Journal of Petroleum Science and Engineering, **43**, 219-239.

Moridis, G., and Collett, T., 2004. Strategies for gas production from hydrate accumulations under various geologic conditions, Proc. Tough Symposium, 2004. Lawrence Berkeley National Laboratory LBNL-52568.

Muraoka, M., Ohtake, M., Susuki, N., Morita, H., Yamamoto, Y., Ohshima, M., Izumi, S., Kumar, P. this issue. Thermal properties of highly saturated methane hydrate-bearing sediments recovered from the Krishna Godavari and Mahanadi basins, Marine and Petroleum Geology.

Myshakin, E. M., Gaddipati, M., Rose, K., Anderson, B. J. 2012. Numerical simulations of depressurization-induced gas production from gas hydrate reservoirs at the Walker Ridge 313 site, northern Gulf of Mexico. Marine and Petroleum Geology, **34**, 169–185.

Nishio, S., Ogisako, E., Denda, A. 2009. Geotechnical Properties of Core Samples Recovered from Seabed Ground in East Nankai Trough, Journal of Geography, **118** (5), 955-968 (in Japanese).

Rutqvist J. and Tsang, C.-F. 2002. A study of caprock hydromechanical changes associated with CO_2 injection into a brine aquifer. Environmental Geology, **42**, 296-305, 2002.

Ryu, B.-J., Collett, T., Riedel, M., Kim, G.-Y., Chun, J.-H., Bahk, J.-J., Lee, J.-Y., Kim, J.-H., Yoo, D.-G. 2013. Scientific results of the second gas hydrate drilling expedition in the Ulleung basin (UBGH-2). Marine and Petroleum Geology, **47**, 1-20.

Servio, P., Englezos, P., 2001. Effect of temperature and pressure on the solubility of carbon dioxide in water in the presence of gas hydrate. Fluid Phase Equilibria, **190**, 127-134.

Shukla, K., Kumar, P., Collett, T., Boswell, R., Frye, M., Riedel, M., Pandey, B., Kaur, I., Vishwanath, K., et al. this issue. National Gas Hydrate Program Expedition 02 in the offshore of India: pre-expedition drill site evaluation in the Krishna-Godavari deep offshore, Marine and Petroleum Geology.

Somerton, W.H., 1992. Thermal properties and temperature related behavior of rock/fluid systems, Development in Petroleum Science, 37.

Torres, M., Trehu, A., Cespedes, N., Kastner, M., Wortmann, U., Kim, J., Long, P., Malinverno, A., Pohlman, J., Riedel, M., Collett, T. 2008. Methane hydrate formation in turbidite sediments of northern Cascadia, IODP Expedition 311, Earth and Planetary Science Letters, **271**, 170-180.

Touloukian, Y. S., Liley, P. E., Saxena, S. C. 1970. Thermophysical properties of matter, - The TPRC Data Series, volume 3.

Uchida, S., Lin, J.S., Myshakin, E. M., Seol, Y., Boswell, R. this issue. Numerical simulation of sand migration in interbedded hydrate-bearing sediments at Site NGHP-02-16. Marine and Petroleum Geology.

Uchida, S., Soga, K., Yamamoto, K. 2012. Critical state soil constitutive model for methane hydrate soil, J. Geophys Res., 117 (B3), B03209.

Uddin, M., Wright, J.F., Dallimore, S.R., Coombe, D. 2012. Gas hydrate production from the Mallik reservoir: numerical history matching and long-term production forecasting, in: Dallimore, S.R., Yamamoto, K., Wright, J.F., Bellefleur, G. (Eds.), Scientific results from the JOGMEC/NRCan/Aurora Mallik 2007-2008 Gas Hydrate Production Research Well Program, Mackenzie Delta, Northwest Territories, Canada. Geological Survey of Canada, Bulletin 601, pp. 261-289.

van Genuchten, M.T. 1980. A closed-form equation for predicting the hydraulic conductivity of unsaturated soils. Soil Sci. Society, **44**, 892-900.

Waite, W.F., Ruppel, C. D., Collett, T. S., Schultheiss, P., Holland, M., Shukla, K. M., Kumar, P. this issue. Multi-measurement approach for establishing the base of gas hydrate stability in the Krishna-Godavari Basin, offshore India, for sites cored during Expedition NGHP-02. Marine and Petroleum Geology, https://doi.org/10.1016/j.marpetgeo.2018.07.026

Waite, W. F., Stern, L. A., Kirby, S. H., Winters, W. J., Mason, D. H. 2007. Simultaneous determination of thermal conductivity, thermal diffusivity and specific heat in sI methane hydrate. Geophysical Journal International, **169**, 767-774.

Yamamoto, K., Kanno, T., Wang, X., Tamaki, M., Fujii, T., Chee, S., Wang, X., Pimenov, V., Shako, V. 2017. Thermal responses of a gas hydrate-bearing sediment to a depressurization operation. RSC Advances, **7** (10), 5554-5577.

Yamamoto, K., Terao, Y., Fujii, T., Ikawa, T., Seki, M. 2014. Operational overview of the first offshore production test of methane hydrates in the Eastern Nankai Trough. OTC-25243-MS. In: Offshore Technology Conference, Houston, TX, 5-8 May.

Yoneda, J., Oshima, M., Kida, M., Kato, A., Konno, Y., Jin, Y., Jang, J., Waite, W. F. this issue-a, Permeability variation and anisotropy of hydrate-bearing pressure-core sediments recovered from India's National Gas Hydrate Program Expedition, NGHP-02. Marine and Petroleum Geology, https://doi.org/10.1016/j.marpetgeo.2018.07.006

Yoneda, J., Oshima, M., Kida, M., Kato, A., Konno, Y., Jin, Y., Jang, J., Waite, W. F. this issue-b, Pressure core based onshore laboratory analysis of mechanical properties of hydrate-bearig sediments recovered during India's India National Gas Hydrate Program Expedition (NGHP)02. Marine and Petroleum Geology, https://doi.org/10.1016/j.marpetgeo.2018.09.005

Yoneda, J., Oshima, M., Kida, M., Kato, A., Konno, Y., Jin, Y., Tenma, N. this issue-c, Consolidation and hardening behavior of hydrate-bearing pressure-core sediments recovered from the Krishna-Godavari Basin, offshore India. Marine and Petroleum Geology, https://doi.org/10.1016/j.marpetgeo.2018.09.021

Yang, S., Liang, J., Lei, Y., Gong, Y., Xu, H., Wang, H., Lu, J., Holland, M., Schultheiss, P., Wei, J. 2017. GMGS4 gas hydrate drilling expedition in the South China Sea. Fire in the Ice, **17** (1), 7-11.

Zheng, S., G.J. Moridis, K. Zhang, R. Yang, N. Wu. 2010. Numerical investigation of gas production strategy for the hydrate deposits in the Shenhu area. OTC 20551. In: Offshore Technology Conference, Houston, Texas, 3-6 May.

Zhou, M., Soga, K., Xu, E., Uchida, S., Yamamoto, K. 2014. Numerical study on Eastern Nankai Trough gas hydrate production test. OTC-25169-MS. In: Offshore Technology Conference, Houston, Texas, 5-8 May.